MODELLING THE DAMAGE EVOLUTION DURING THE MACHINING OF A PARTICLE REINFORCED METAL MATRIX COMPOSITE.

Declan Brazil & John Monaghan

Department Of Mechanical & Manufacturing Engineering
Parsons Building
Trinity College Dublin

ABSTRACT

This paper reports on a numerical test program to model sub surface damage resulting from the machining of a particle reinforced metal matrix composite (PRMMC's). The composite material modelled was a 35% SiC particle reinforced A356 Aluminium alloy. A sub modelling approach was adopted in order to analyse the problem. Simulation of the metal cutting process was performed using FORGE2, an elasto-visco plastic FEA code. The sub modelling of the PRMMC was performed using ANSYS 5.2, an elasto-plastic FEA code. The machining model was done using the aluminium alloy without the reinforcement and the results from FORGE2 were used as inputs for the ANSYS sub models of the composite material. A quantitative wear model was constructed in order to establish the detrimental effect of SiC on a tungsten carbide cutting tools during machining of PRMMC's. All FE models where assumed to be plane strain. The results of the FE sub modelling agree favorable with those observed under scanning electron microscaope (SEM). Void growth rates appear to be extremely sensitive to inital defects in the microstructure. Particle clustering also has a detremential effect on the rate of void growth. It was observed that SiC particles under the action of normal loads cause intensive normal stresses at the ponit of contact with tungsten carbide. Overstraining of the matrix envolopes the particle in contact for both normal and tangential loadings.

1.0 INTRODUCTION

Metal Matrix Composites (MMC's) are a range of materials that offer desirable mechanical and physical properties to design engineers. MMC's comprise a soft ductile matrix material, such as aluminium, reinforced by a hard ceramic second phase. The reinforcing phase can have various morphologies, which include particle, fibre or whisker. Generally, MMC's contain only one of these reinforcements but hybrid composites have been made [1]. Particle reinforced MMC's are the cheapest to produce and offer high strength to stiffness ratio's coupled with light weight. Over the last 25 years considerable effort has been directed to produce ductile damage free PRMMC components and detailed reviews of many of these techniques are availible in published literature[2]. Differences in the coefficient of thermal expansions between the matrix and the reinforcement results in residual stresses due to the temperatures generated during production and machining. These residual stresses are tensile in the matrix material and compressive in the reinforcement [3]. Such stresses can be detrimental to the rate of fatigue crack propagation and void nucleation.

Due to the expense of producing MMC components, near net shape processing is suggested as the most desirable production route for such components. Consequently components such as cylinders and pressure vessel covers have been net shape processed [4]. However, even after forming a component using a near net shape processes a finish machining operation is required. While near net shape processing reduces the overall cost of production

it is often hard to obtain acceptable surface finish and dimensional tolerances, hence the necessity for a finish machining operation. Machining of MMC's is very difficult due to the abrasive nature of the ceramic reinforcement on the cutting tool. Machining with conventional tooling such as tungsten carbide or coated tungsten carbides in not possible when surface finish and dimensional stability is required due to excessive tool wear [5]. This excessive tool wear causes the nose of the cutting tool to become flat and the normal cutting action reverts to a rubbing / burnishing of the material which can generate sub surface damage [6] i.e. void formation and coalesence, as shown in Figure 1.

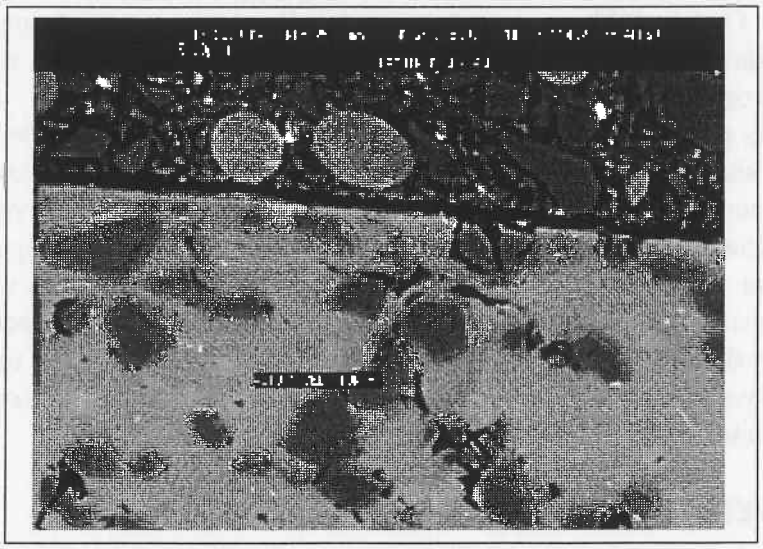

Figure 1. Subsurface Damage Resulting from Machining With Tungsten Carbide

The primary aim of finish machining is to achieve good surface finish coupled with good dimensional tolerance. The cutting parameters such a spindle speed and feed rate have also being found to influence both tool wear and sub surface damage [6]. All these factors coupled with the additional complication of various cutting tool geometries makes the selection of optimal machining parameters and tooling a difficult task. However it is preposed that through the use of FEA such a selection procedure can be made easier.

To date Finite Element Modelling (FEM) of metal cutting has been primarily concerned with 2-D orthogonal cutting with continuous chip formation of single phase materials. There have being some exceptions, such as the work done by Hasemi et al [7] or Marusish and Ortiz [8] which concentrated on segmental chip formation during high speed machining. Segmental chip formation involves a process of shear localisation in which micro cracks are propagated along a shear plane. The simulation of discontinuous chip formation requires a suitable fracture criterion based on mixed mode crack growth model. The actual metal cuttting process involves a combined thermo-mechanical analysis in order to accurately model stress distributions within the work piece and the tooling. Machining involves the generation of a new surface as a result of material flow. Strenkowski and Carroll [9] and other researchers assumed a predefined parting line at which the machined surface would be generated. This type of analysis was based on the theory that at a critical stress (or strain) a node ahead of the approaching cutting tool would split and allow a new surface to be generated. This type of approach is hard to accept since it assumes that separation occurs along a predefined path which does not often occur during a real machining process. Particular models such as that of Shih et al [10] have been fine tuned with experimental results, based on residual stresses in the machined surface, so that the point at which node splitting occurs yields the correct result. However, this model was tailored for a particular material, cutting condition and tool geometry

and therefore does not provide the versatility required for a more generalised industrial application. For complete versatility of FE modelling applied to metal cutting an adaptive non-linear re-meshing algorithm is required. In recent years a few researchers have adopting non-linear re-meshing algorithms into their FE code, for example Chenot and Shenkon [11] used a Delaunay - Voronoi type algorithim.

Modelling the machining of a PRMMC is extremely difficult due to the amount of computational time required. The main difficulty is in establishing a link between the micro and macroscopic processes occurring simultaneously during the machining process of PRMMC's. One possible option is to model the machining of a single phase material and submodel regions throughout the chip and the machined surface with metal matrix composite. The results from the machining model as inputs to the sub model.

In this paper, the FORGE2 code has been used to simulate the steady state machining of the A356 aluminium alloy. The code has full non-linear adaptive remeshing capability based on a Delaunacy-Voronoi type algorithm [12]. No prior assumptions regarding chip geometry or material flow were made. The material thermal and mechanical properties used in the model resulted from experimental work, or literature. The sub models were carried out using ANSYS revision 5.2. Results from the machining model were recorded at six locations starting from the unmachined surface through the shear zone and on to the machined surface. Quantitative wear models were analysed using the ANSYS code. These models used a section of MMC which was loaded into and along a tungsten carbide face.

2.0 FINITE ELEMENT MODELLING

2.1 Machining FEA

The cutting tool chosen for the model was a TNMA tungsten carbide insert with a nose radius of 0.8mm. The tool geometry was drawn in AutoCad R12 and subsequently imported into the FORGE2 package in IGES file format. The cutting speed used for the simulations was 100 m/min and the depth of cut was set to 1mm. Material properties for both the cutting tool and the workpiece are given in Table 1 below.

	Aluminium(Workpiece)	Tungsten Cardibe (Tool)
Young's Modulus , E	74.63 GPa	640 GPa
Poissions Ratio, ν	0.3	0.26
Strain Hardening Term, a	1.13	--
Sensitivity to Strain Hardening, n	0.31	--
Strength Coefficent, K	39.09 GPa	--
Density, ρ	2700 Kg/m^3	15,100 kg/m^3
Thermal Conductivity, k		90 W/mK
Specific Heat Capacity, c_p	237 W/mK	210 J/kgK
Heat Transfer Coefficent, h	9 W/mK	6 W/mK
Coulomb Coefficent of Friction, μ	0.5	0.5
Tresca Coefficent of friction, m	0.2	0.2

Table 1. Listing of Material Properties for Machining Simulation

2.1.1 Computational Considerations

The problem was treated as a coupled thermo-mechanical analysis. The metal and heat flow problems were solved independently at each time step. The results of the material flow where used to update the work piece geometry, while internal heat generation by viscoplastic work and frictional sliding enabled fresh computation of the material properties. The flow

stress of the material is dependent on the strain, strain rate and the temperature of the work piece. The material flow stress is represented by the equation [13]:

$$\sigma_o = \sqrt{3}\,K(\varepsilon, \dot{\varepsilon}, T) \tag{1}$$

The term K(ε, ε, T) is termed the consistency of the material and as can be seen from equation (1) that it depends on the strain and temperature of the material. A linear power strain hardening law was assumed for the material. We may write the consistency in terms of the linear power hardening law as follows [13]:

$$K(\varepsilon, \dot{\varepsilon}, T) = \mathrm{K}_o(1 + a\varepsilon^n)\dot{\varepsilon}^m f(T) \tag{2}$$

K_o is the strength coefficient, a is the strain hardening term, n is the sensitivity to strain hardening and m is the sensitivity to strain rate. f(T) is the dependency of the flow stress on temperature. Both Young's Modulus, E and Poisson's ratio, ν had a linear variation with temperature, given by:

$$E = E_o(1 + aT) \qquad\qquad \nu = \nu_o(1 + aT) \tag{3}$$

where E_o and ν_o are Young's Modulus and Poisson's ratio at room temperature respectively. T is the temperature and a is a temperature term. Combining these two linear temperature laws with equation (2) gives a expression for the consistency of a Elasto-plastic solid:

$$K(\varepsilon, \dot{\varepsilon}, T) = K_o(1 + a\varepsilon^n)(1 + aT)\dot{\varepsilon}^m \tag{4}$$

Contact between the cutting tool and the work piece was characterised by a combined Coulomb and Tresca type friction law. The Tresca friction law is given by equation (5) and represents the shearing created by velocity differences between the cutting tool and the work piece

$$\tau = -m\frac{\sigma_o}{\sqrt{3}}\frac{\Delta V}{\Delta v} \quad \text{or} \quad \tau = -mK(\varepsilon, T)\frac{\Delta V}{\Delta v} \tag{5}$$

m is the friction coefficient and ΔV represents the difference between the velocity of the work piece and the tool. The Coulomb friction law is defined by:

$$\tau = \mu\sigma_n \quad \text{if} \quad \mu\sigma_n < \frac{\sigma_o}{\sqrt{3}} \tag{6}$$

$$\tau = \frac{\sigma_o}{\sqrt{3}} \quad \text{if} \quad \mu\sigma_n > \frac{\sigma_o}{\sqrt{3}} \tag{7}$$

σ_n is the normal stress, σ_o is the flow stress and μ is the friction coefficient. The temperature evolution in the continuum is a result of the competition between the phenomena of internal heat conduction and internal heat dissipation. The heat balance equation of the continuum may be written as:

$$\rho c\frac{\partial T}{\partial t} = \mathrm{div}\left(k\,\mathrm{grad}T\right) + \mathrm{W} \tag{8}$$

The first term represents the temperature evolution, the second term represents internal conduction and the last term represents the internal heat generation by viscoplastic deformation. The internal heat generation was calculated using a Norton-Hoff law:

$$W = \eta K \sqrt{3}\, \dot{\varepsilon}^{m+1} \tag{9}$$

η is the deformation efficiency, K is the consistency , ε is the strain rate and m is the sensitivity to strain rate. The thermal phenomena occurring during machining are summarised is graphical form in figure 2.

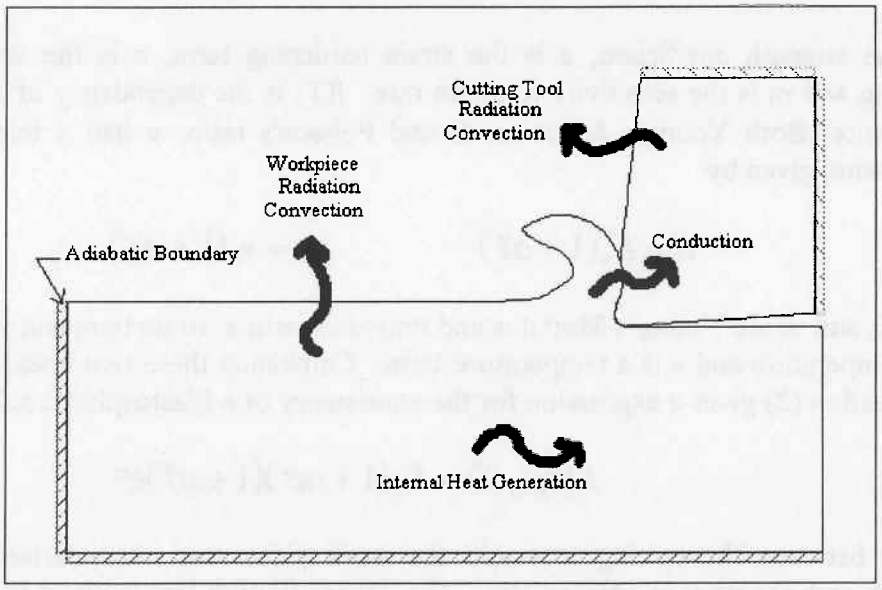

Figure 2. Flux Paths Accounted For During Machining Simulation

Frictional heat flux at the tool / work piece interface is shared according to their respective effusivities. The effusivity of a component may be calculated by the expression

$$b = \sqrt{k * \rho * c_p} \tag{10}$$

k is the conductivity of the material, ρ is the density of the material and c_p is the specific heat capacity. The heat generated by frictional sliding is represented by the expression

$$\phi_{fr} = \frac{b_1}{b_1 + b_2} * \alpha * K * \Delta V^{p+1} \tag{11}$$

b_1, b_2 is the tool and material effusivites respectively, α is the heat transfer coefficient between the tool and the material (assumed to be the average of the tool and work piece conductivity), p is equal to the sensitivity to strain, K is the consistency, and ΔV is the difference in velocity between the tool and the work piece.

2.2 Sub Modelling FEA

The sub models of various zones of the workpiece were based on a 100μm square region with a 35% by volume SiC particle reinforcement. These regions were obtained from SEM images of a section of the machined workpiece. Unlike previous FEA work done on

PRMMC's [14] the particle morphology chosen was that of an actual MMC microstructure rather than of an idealised ordered array of circular or square shapes. The average particle size of 13μm, with a mean aspect ratio of 3:1. The 100μm micrograph of the microstructure was imported into ACAD R12 in GIF format and it was subsequently traced over on a new layer. The trace was finally imported into ANSYS 5.2 in IGES file format. The 100μm micrograph and the ACAD tracing are shown in figure 3.

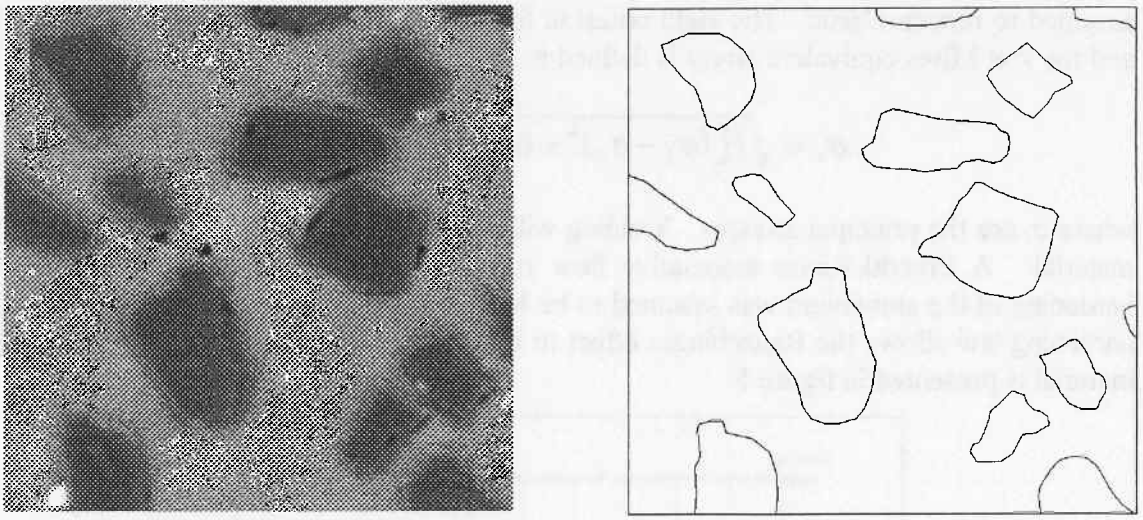

Figure 3. 100μm MMC Micrograph & ACAD Tracing Of Micrograph

In modelling an actual microstructure stress concentrations associated with sharp particle corners [15] can be modelled. The imported drawing of the model was meshed using 6-noded triangular elements and restrained in finite element space by 8 spring elements positioned at the 4 other corners of the model, figure 4.

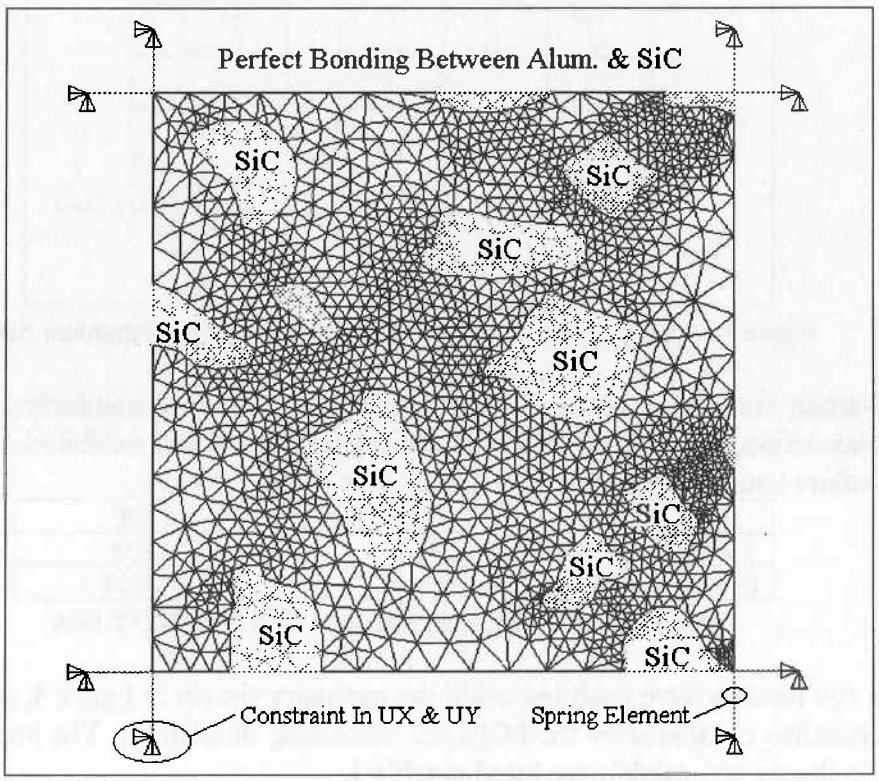

Figure 4. Mesh Of Sub Model Using 6-Noded Triangular Elements

The springs were given a very low stiffness to prevent any artificial stress concentrations during the computation. This type of restraint was imposed for two reasons, firstly to prevent rigid body motion of the model and secondly to avoid any artificial stress concentrations being created in the corners of the model, which would arise if normal degree of freedom constraints were used.

The aluminium alloy was able to deform plastically while the SiC particles were assumed to remain elastic. The yield criterion for the aluminium was the von Mises criterion, and the von Mises equivalent stress is defined as:

$$\sigma_e = \sqrt{\tfrac{1}{2}\left[(\sigma_1 - \sigma_2)^2 + (\sigma_2 - \sigma_3)^2 + (\sigma_3 - \sigma_1)^2\right]} \qquad (13)$$

where σ_i are the principal stresses. Yielding will occur when σ_e exceeds the yield stress of the material. A Prandtl-Reuss associative flow rule was assumed for the aluminium and the hardening of the aluminium was assumed to be Multi-linear Kinematic Hardening. This type of hardening law allows the Bauschinger effect to be represented. The stress strain curve for the material is presented in figure 5.

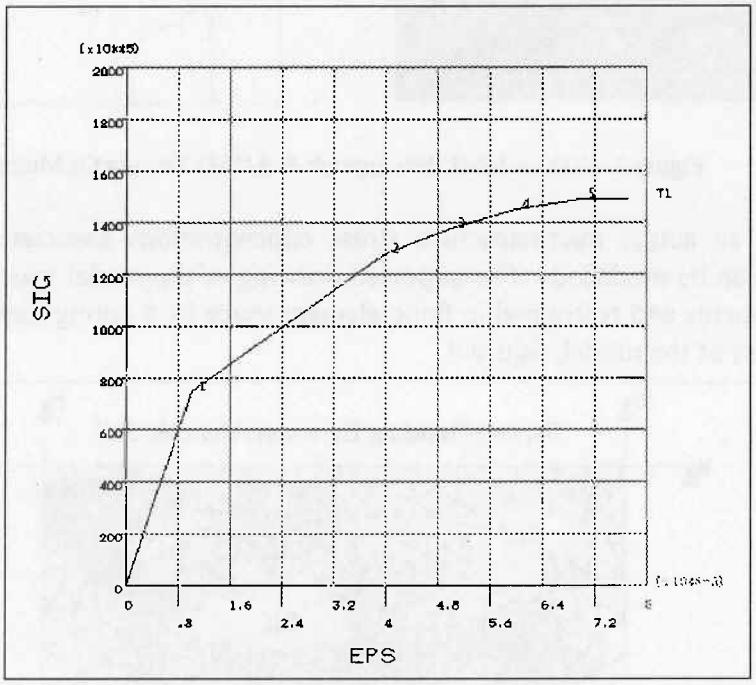

Figure 5. Approximated FE Stress/Strain Curve For A356 Aluminium Alloy

The stress-strain curve was obtained from tensile tests on the unreinforced matrix material. The SiC was defined by Young's Modulus and Poisson's ratio and exhibited no plasticity. The numerical values used in the simulations are given in Table 2 below.

	Alumium A356	SiC
Youngs Modulus (GPa)	74.63	450
Poission's Ratio	0.3	0.17

Table 2. Elastic Mechanical Properties Used For ANSYS FEA

Six sub models were analysed using the geometry shown in figure 4, the imposed loads were the pressures calculated by the FORGE2 machining simulation. The imposed hydrostatic pressures on the six sub-models are listed in table 3.

Location	1	2	3	4	5	6
Pressure FORGE2 (MPa)	20	52.7	69.6	-4.78	59.1	-24.7
Corrected Pressure (MPa)	26.9	70.77	93.46	-6.42	-79.4	-33.2

Table 3. Hydrostatic Pressure Loadings Applied To Submodels

The pressures actually applied to the sub models were larger than those outputted from FORGE2 as can be seen in table 3. These pressures are magnified by a factor of 1.34, this magnification factor was obtained by comparing the tangential cutting forces resulting from cutting force tests performed on both the A356 unreinforced alloy and an the SiC particle reinforced A356 alloy. The resulting tangential cutting forces was 350N and 470N for the unreinforced and reinforced alloy respectively. The pressures where applied in sequential load steps. Figure 6 shows the hydrostatic pressures generated by the FORGE2 simulation. The locations for the six sub models were chosen to lie along a line was just below the machined surface, as shown in figure 7. The reason for selecting this location was in order to estimate the sub surface damage attributed to the machining process.

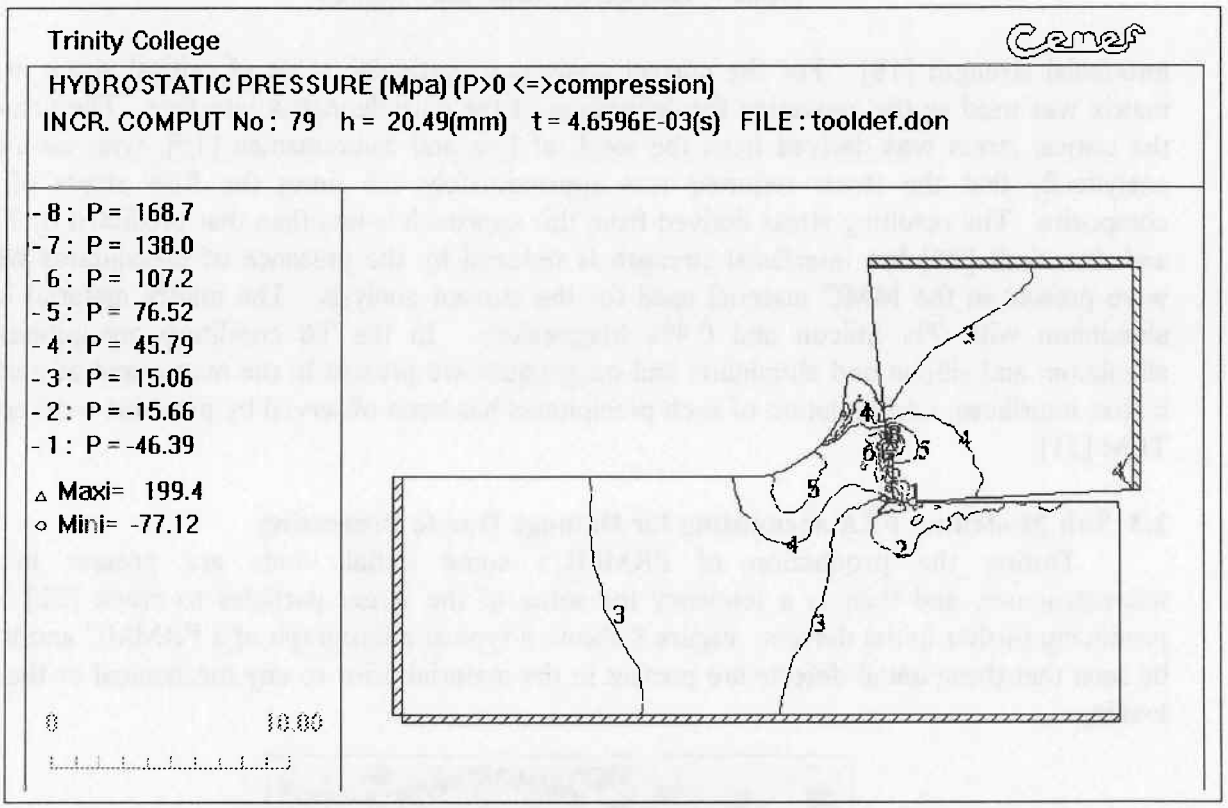

Figure 6. Hydro Static Pressures Outputted From FORGE2 Simulation

In order to monitor accumulating damage in the composite during machining a element kill method was utilised at the end of each load step so as to simulate particle matrix debondingand void growth. This method reduces selected elements stiffness by a factor of $1x10^{-6}$. The actual stress / strain condition at which particle/matrix debonding occurs is very difficult to define. It is believed that the debonding process occurs over a range of strain rather than at one particular strain [16]. For the current simulations however a defined value for particle/matrix debonding was required in order to activate the element kill procedure.

Cavity nucleation is a process involving both stress and strain energy release, it can be assumed that there exists some threshold strain value of the far feild strain below which there is insufficient stress to debond the interface, or elastic strain energy available for the creation of a new surface. Various models exist based on both strain energy release rates [17], and

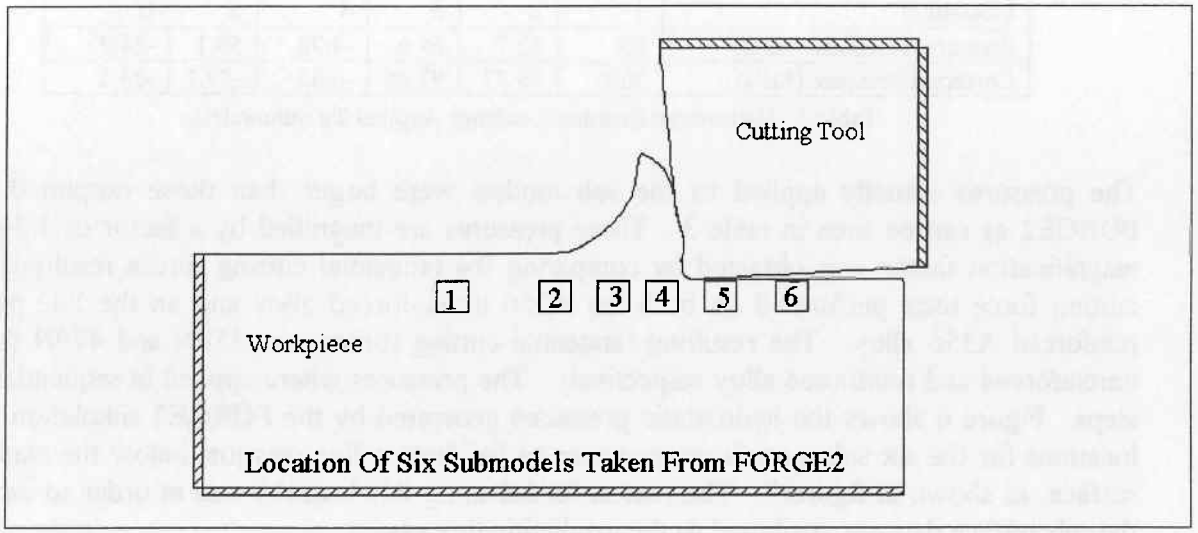

Figure 7. Location Of Submodelled Regions

interfacial strength [18]. For the current analysis a particular value of critical strain in the matrix was used as the activation for debonding of the particle/matrix interface. The value of the critical strain was derived from the work of Lee and Subramanian [19], who estimated analytically that the stress required was approximately 1.5 times the flow stress of the composite. The resulting stress derived from this approach is less than that predicted by Flom and Arsenault [20] but interfacial strength is reduced by the presence of precipitates which were present in the MMC material used for the current analysis. The matrix material is an aluminium with 7% Silicon and 0.4% Magnesium. In the T6 condition precipitates of aluminium and silicon and aluminium and magnesium are present in the matrix and at particle matrix interfaces, accumulation of such precipitates has been observed by previous workers by TEM [21].

2.3 Sub Modelling FEA accounting for Damage Due to Processing

During the production of PRMMC's some initial voids are present in the microstructure, and their is a tendency for some of the larger particles to crack [22], thus producing further initial defects. Figure 8 shows a typical micrograph of a PRMMC and it can be seen that these initial defects are present in the material prior to any mechanical or thermal loading.

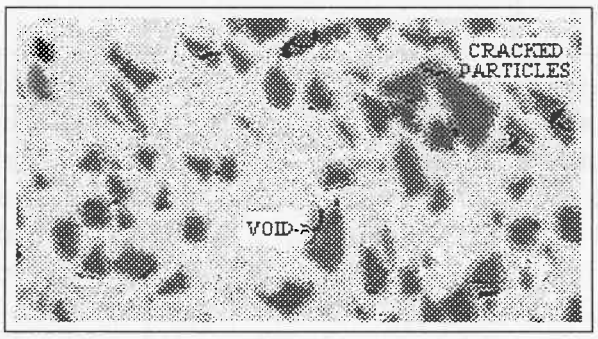

Figure 8. Micrograph Showing Particle Reinforced MMC With Initial Defects

To account for these initial defects a second set of sub models was produced for analysis which contained microstructural defects. Figure 9 shows the mesh used for these sub-models, the locations of the sub-models are the same as before, figure 7. The element kill procedure was activated between each subsequent load step.

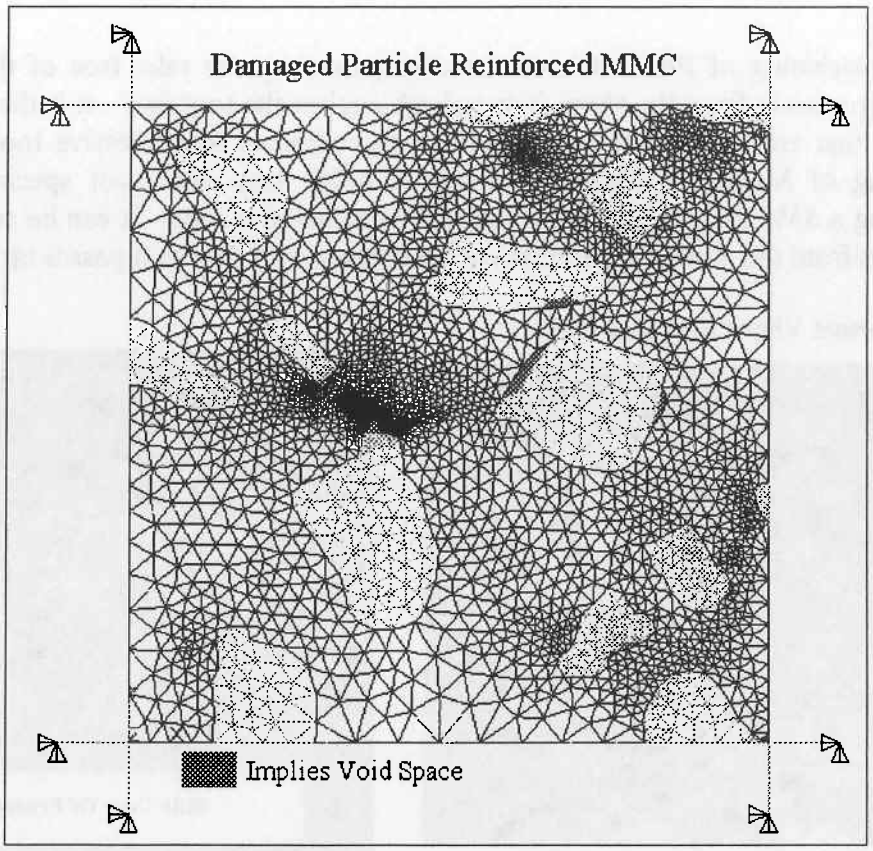

Figure 9. Damaged PRMMC Mesh Using 6-Noded Triangular Elements

2.4 Finite Element Models For Wear Analysis

The finite element models used to simulate the wear action occurring during the machining of PRMMC's gave a quantitative overview of the abrasive mechanisms which results in excessive tool wear. The main type of wear mechanism associated with machining of PRMMC's is that of three body abrasion [23]. Figure 10 shows a typical CBN cutting tool edge after machining a 35% SiC particle reinforced A356 aluminium alloy composite. The wear pattern on the tool can be seen to have been produced by abrasion.

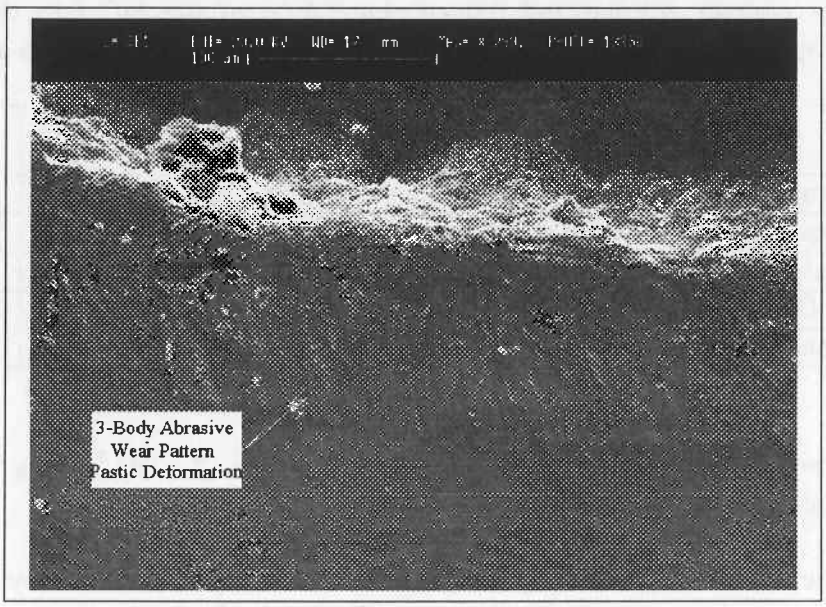

Figure 10. Abrasive Wear Pattern On Cubic Boron Nitride (CBN) Cutting Tool

During machining of PRMMC's as the chip passes up the rake face of the tool some SiC particles protrude from the aluminium and rub against the tool face. It is these protruding SiC particles that are believed to be the driving force behind the excessive tool wear during the machining of MMC's. Figure 11 shows a quick stop chip root specimens taken while machining a 35% SiC particle reinforced A356 aluminium alloy. It can be seen that some SiC protrudes from the aluminium and will make contact with tool as it passes up the rake face.

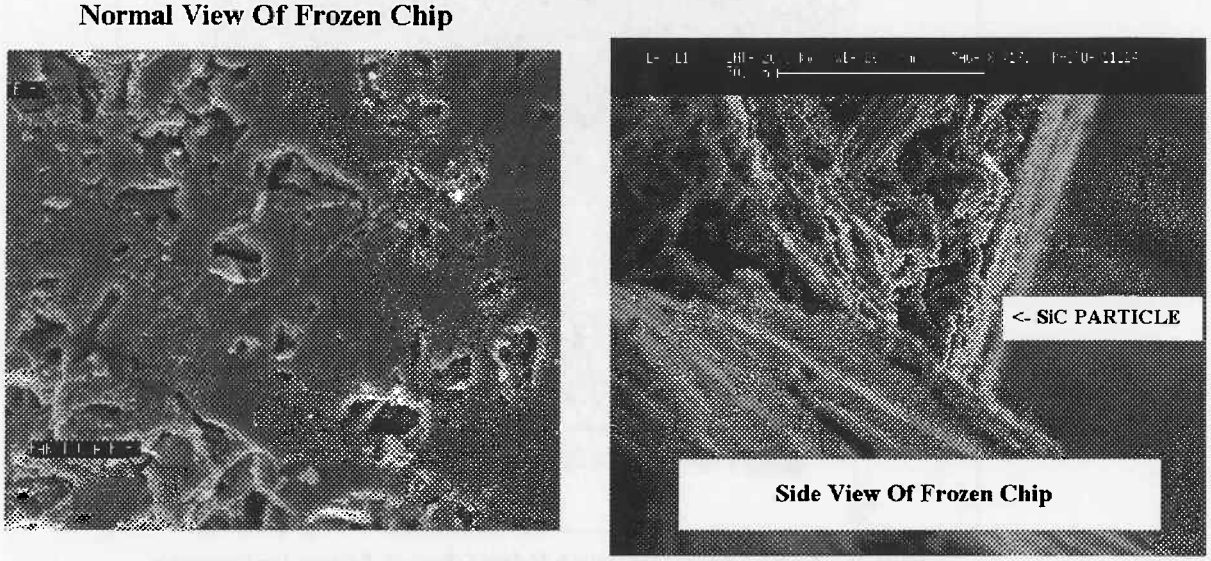

Figure 11. Normal & Side View Of Frozen Chip Obtained From A Quick Stop Device

The model used for this section of the analysis can be seen in figure 12. As shown in figure 12 the 100μm square of MMC was constrained / displaced on three of its sides. The tungsten carbide tooling was constrained in the X and Y-direction along both of its sides and bottom edge for both load steps. The tool material is described by a rectangle and the material properties were those of tungsten carbide. The tool material was assumed to deform elastically. Contact elements were generated between the MMC and the tool material to account for contact stresses and reduce penetration of the SiC into the tool. Details of material properties and real constants for each of the element sets is given in table 4.

	TYPE	BEHAVIOUR	YOUNG'S MODULUS	POISSON'S RATIO	STIFFNESS
Matrix Element	6-Noded	non-linear	74.63	0.3	-------
Reinforcement	6-Noded	Linear	450	0.17	-------
Cutting Tool	6-Noded	Linear	640	0.26	-------
Contact	3-Noded	non-linear	-------	-------	Normal 50E10
Spring Element	2-Noded	Linear	-------	-------	Long. 97,000

Table 4. Material & Element Properties For Wear Analysis

The constraints placed on the model are shown in figure 12. The loading simulated during the wear analysis was divided into 2 sequential load steps.

- The MMC was displaced normally into the tungsten carbide by 2.5μm. The MMC was not allowed to displace horizontally during this load step.
- In the second load step the MMC was restrained in the vertical direction and displaced horizontally 2.5μm.

These load steps where applied in effort to simulate a loading similar to that experienced during machining.

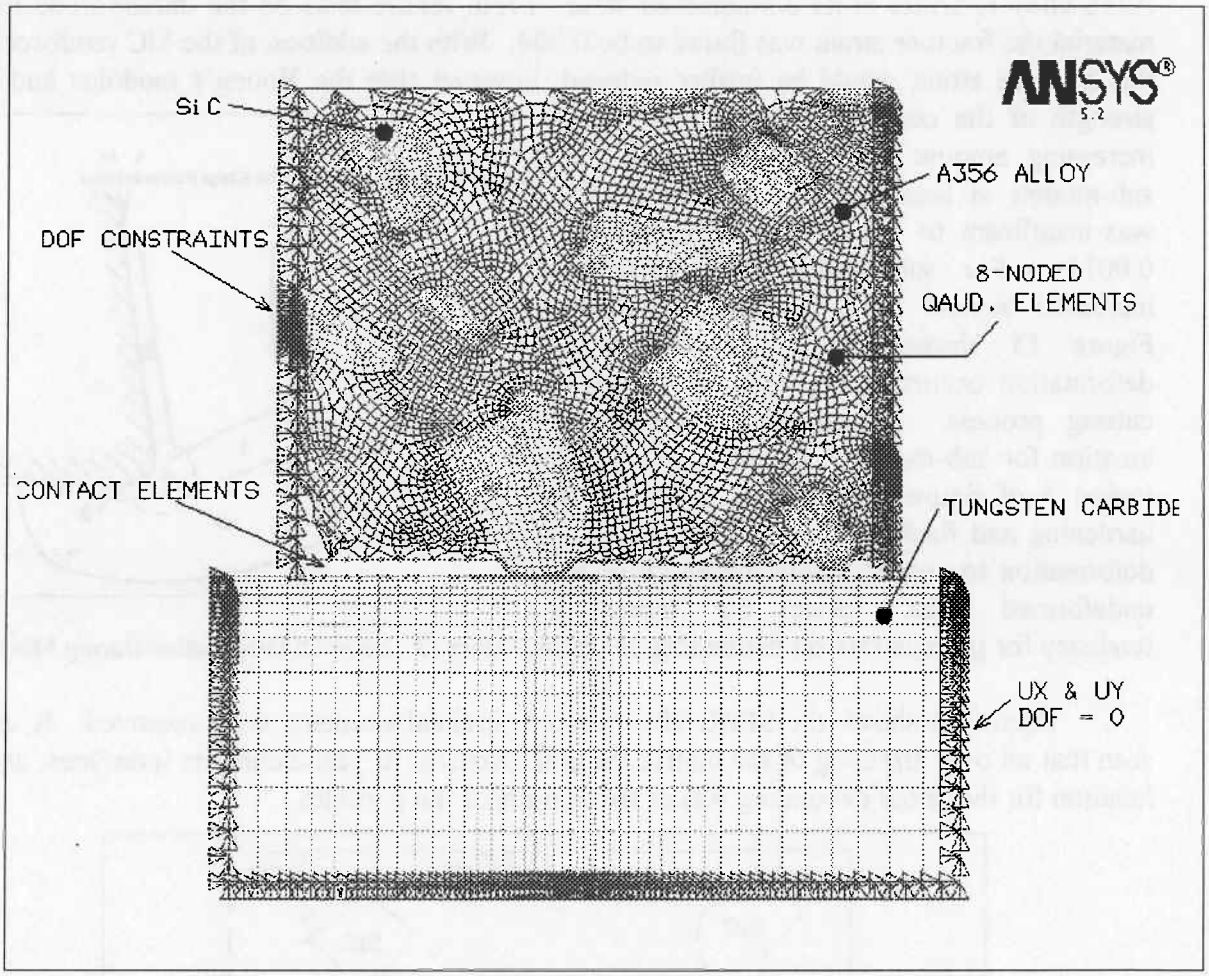

Figure 12. FE Model Used For Wear Analysis

3.0 RESULTS & DISCUSSION

3.1 Damage Free FE Models With Perfect Particle / Matrix Bonding

During the analyses of all six of the sub-models an element kill macro was active. This meant that once the strain in any element was greater or equal to the critical value of 0.0014 the element stiffness was reduced by a factor of $1x10^{-6}$. This value of the critical or 'death' strain is reasonable considering the brittle nature of the MMC material and also because an A356 alloy is brittle in its unreinforced state. From tensile tests on the unreinforced matrix material the fracture strain was found to be 0.004. With the addition of the SiC reinforcement this fracture strain would be further reduced, however that the Young's modulus and flow strength of the composite decrease with and increasing amount of porosity (voids). For sub-models at locations 1 and 2 the loading was insufficent to cause matrix strain beyond 0.0014. For sub model 3 the straining increased beyond 0.0014 in some elements. Figure 13 shows the various zones of deformation occurring during a normal metal cutting process. It can be seen that the location for sub-model 3, figure 7, lies within region 5 of figure 13. In this region strain hardening and flank face contact cause plastic deformation to spread below the depth of the undeformed chip, hence the increasing tendency for particle /matrix debonding to occur.

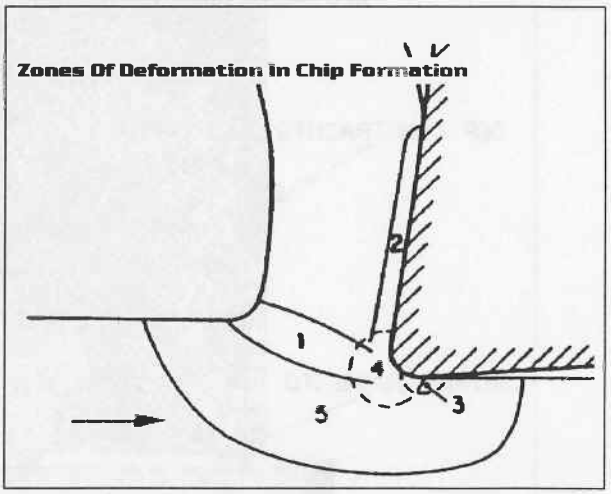

Figure 13. Zones Of Deformation During Machining

Figure 14 shows the MMC after the overstrained elements were removed. It can be seen that all over straining of the matrix material occurred at particle/matrix interfaces, and the location for the initial debonding was at the corners of the particles.

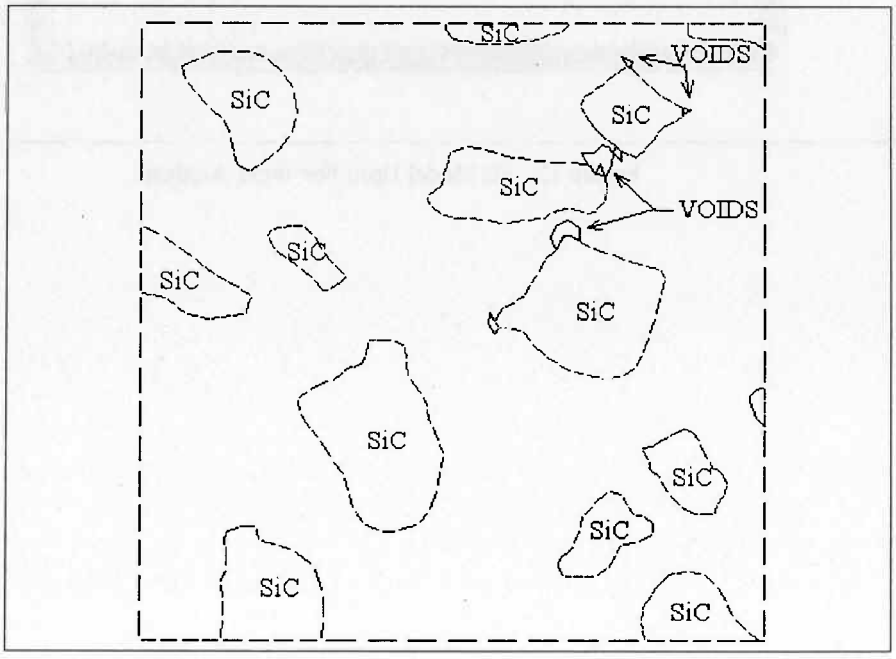

Figure 14. Void formation Due To Applied Loading At Sub-Model Location 3

Another location for particle/matrix debonding was along flat surfaces where high tensile hydrostatic pressures caused matrix cavitation at the particle/matrix interface. (The degree of debonding is dependent on the bond strength.) Figure 15 shows the void growth/formation at sub-model location 5. It can be seen that at this location where further

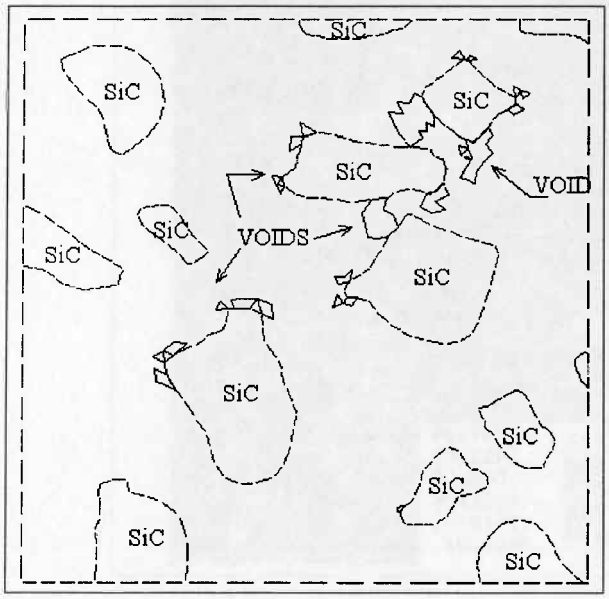

Figure 15. Void Formation For Sub-Model 5

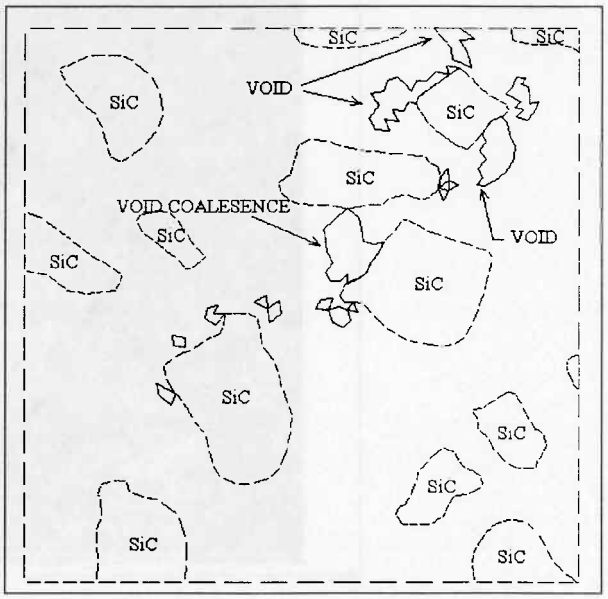

Figure 16. Void Formation For Sub Model 6

stressing is expected to occur due to the rubbing action of the cutting tool on the machined surface. It can be seen that the initial voids have grown in size. Also, new voids have initiated at regions where the matrix has yielded. These regions, as before, are at the particle corners and at flat surfaces. These results are in agreement with the work of Lee and Subramanian [24], who investigated a the problem of a plate with a central inclusion using Airy stress functions. Their solution for the circular inclusion predicted that particle/matrix debonding would occur at the poles of the inclusion. However, with the irregular shaped particles used in the current analysis the high local stresses developed at the particle corners may be relieved by microscopic plastic flow whereas high hydrostatic stresses developed at the flat interfaces normal to the applied loading are more likely to induce voiding, figure 15-16. Figure 16 shows the accumulated damage at sub-model location 6. It can be seen that the process of void nucleation, propagation and coalescence has occurred to produce subsurface damage associated with the machining PRMMC's with tungsten carbide. Propagation of voids appears to be either void-to-void coalescence, depending on particle spacing, or due to voids that nucleate around the particle matrix interface if isolated from other particles.

Along flat particle/matrix interfaces high hydrostatic stresses develop, figure 17 shows the hydrostatic stress state associated with sub-model location 1. Numerically the values are quite low due to the nature of the loading, but the location for the high stresses is as anticipated. Particle reinforced MMC's have been seen to be sensitive to superimposed levels of hydrostatic pressures [25]. It has known that superimposed levels of compressive hydrostatic pressures reduce the damage accumulation rate. The compressive hydrostatic pressures act to close voids, a similar analogy may be made to that of compressive stresses causing fatigue crack closure, this can be seen for the compressive loading of sub-models 1 to 3 where minimial void growth occurred, figure 14. When the hydrostatic loading changes from compressive to tensile in nature, i.e. moving from region 3 to 4, the initial voids are opened up and coalesce with

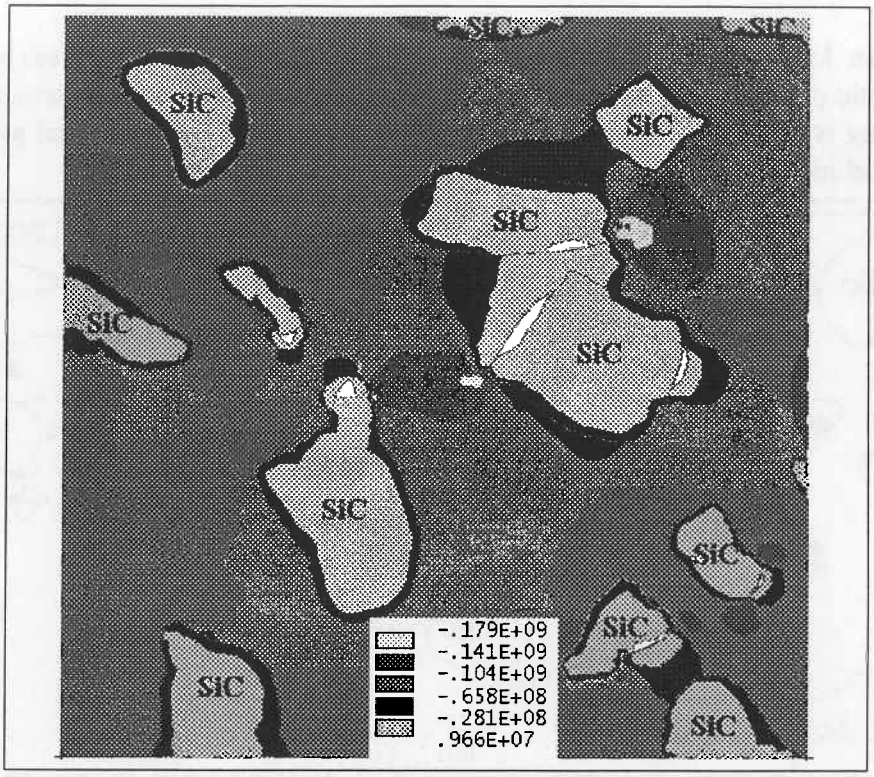

Figure 17. Hydrostatic Stress Plot At Sub-Model Location 1

surrounding voids. It is appears that it is in this region that the majority of damage occurs when machining PRMMC's. Comparing the void patterns in figures 15 and 16, it can be seen that damage still accumulates under the action of a reducing tensile loading (from 79 MPa in location 5 to 33 MPa in region 6).

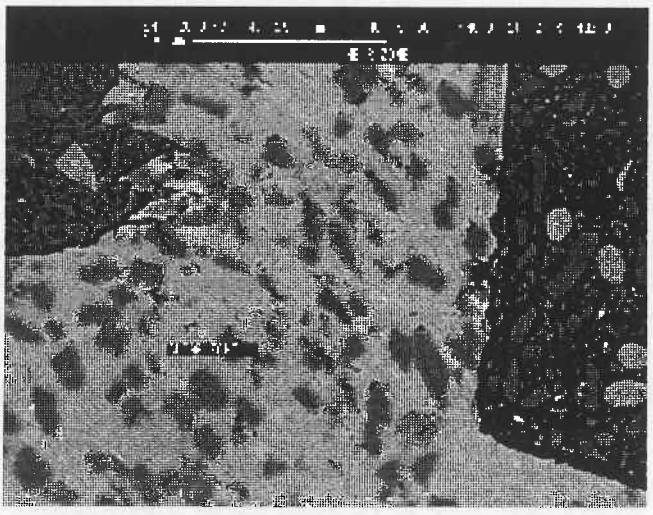

Figure 18. Sub-Model Location 3

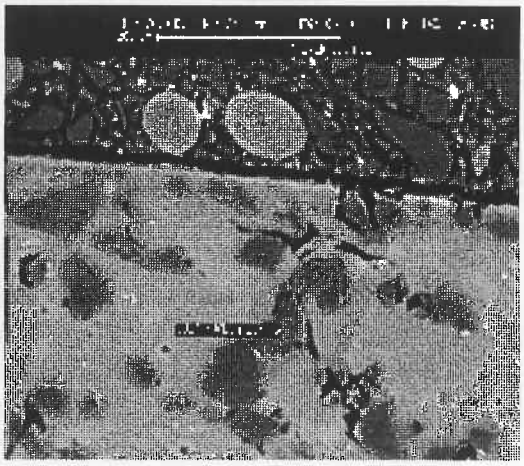

Figure 19. Sub-Model Location 6

Figure 18 shows a chip root sample obtained when machining with a tungsten carbide tool. The location of these micro-graphs allows a comparison to be made between the predicted damage occurring in sub-model 3 and the actual subsurface damage shown in figure 18. Figure 19 is a machined surface micro graph taken from a location which approximates to the location of sub-model 6. It can also be seen in figure 18 that in the area in front of the chip

very little voiding has occurred. A comparison of this region can be made with sub-model 2. From the current FE simulations this region suffered very little damage, i.e. the maximum strain in the matrix did not exceed the prescribed failure strain.

As a result of processes used to manufacture PRMMC's particle clustering occurs, as shown in figure 8. These regions of particle clusters are sites for accumalted/premature damage. This is verified by both the current finite modelling and by micro graphs of actual loaded composites, figure 18. Particle clustering causes a larger perturbation in the matrix flow then for the case of single isolated particles. Another feature associated with particle clustering is the rise in magnitude of the stresses between the particles. This occurs because

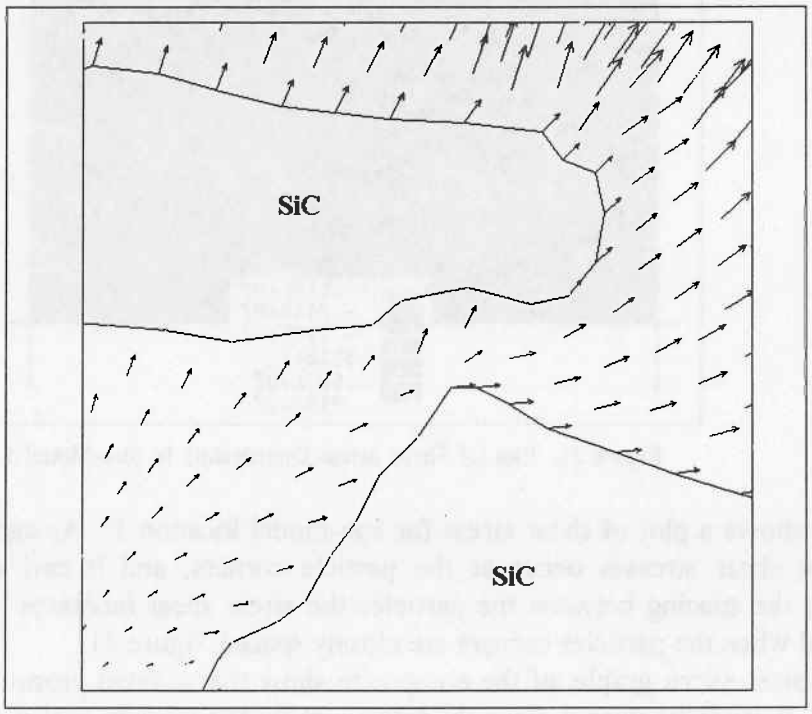

Figure 20. Translation Vector Plot Between Two SiC Particles

matrix flow is inhibited, as shown in figure 20 which presents velocity vectors plotted for the sub model at location 5. The length of the vectors corresponds to the magnitude of the velocity at that point. It can be seen that entering the region between the two SiC particles the flow of the matrix is reduced and subsequently increases again leaving the particles. A simplified analysis of a piece of material between two rigid particles can illustrate this stress intensification phenomena. Assuming the aluminium layer is of thickness h and length b and sticking friction to exist between the rigid particles and the matrix material the magnification of the stress may be expressed by [26]

$$\sigma_{mag} = \sigma_{flow}\left(1 + \frac{b}{2h}\right) \tag{14}$$

where σ_{mag} and σ_{flow} are the magnification in stress and the flow stress respectively. If h = b the stresses are three times the flow stress generated. A slip line feild approach to the same problem gives a slightly different magnification factor but still dependent on the thickness and length [27]

$$\sigma_{mag} = \sigma_{flow}\left(\frac{3}{4} + \frac{b}{4h}\right) \tag{15}$$

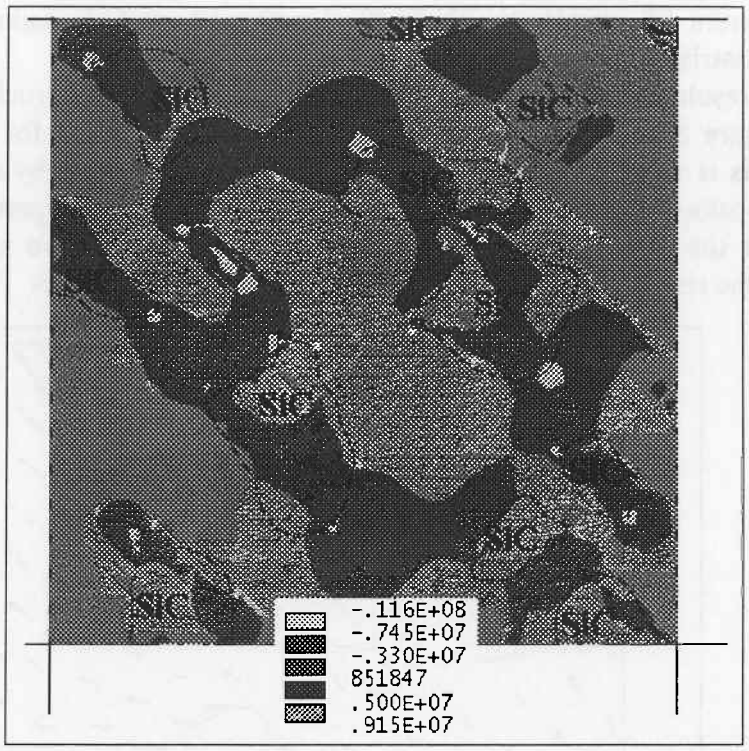

Figure 21. Plot Of Shear Stress Distribution In Sub-Model 1

Figure 21 shows a plot of shear stress for sub-model location 1. As can be seen in figure 21 the largest shear stresses occur at the particle corners, and it can also be seen that by decreasing the spacing between the particles the stress shear increases. The stress is further aggravated when the particles corners are closely spaced, figure 21.

Typical micro graphs of the composite show that a small proportion of particles have fractured. Particle fracture is strongly dependent on the particle aspect ratio [28]. Assuming that the load is transferred to the reinforcement by interfacial shear stresses it can be shown that the shortest fibre that can be stressed to its failure strength, σ_I, has an aspect ratio given by

$$S \simeq \frac{\sigma_I}{2\tau_{MY}} \simeq \frac{\sigma_I}{\sigma_{MY}} \qquad (16)$$

where τ_{MY} and σ_{MY} are the shear and yield strength of the matrix alloy respectively. Taking a high matrix yield stress of 300 MPa and a low reinforcement strength of 3 Gpa gives an aspect ratio of 10. This solution is derived from a shear lag model [29] and ignores any plastic relaxation processes that may occur at sharp corners which would reduce the reinforcement stress further. The fractured particles shown in the micro graphs generally are a result of the manufacturing processes. However, particle fracture does occur within elongated particles or when a strong bond exists. Figure 22 shows principal stress vectors in a loaded particle. The length of the arrow indicates the magnitude of the principal stress at that location. At the aft of the particle where two sharp corners are close together the principal stresses are large and the vectors are aligned so as to cause crack opening if a small defect where to exist in the ceramic. Due to the brittle nature of ceramics microscopic defects are common. If a defect was in this region of high principal stress the particle would fracture and cause the formation of a void which could in turn coalesce with other voids and cause failure of the composite.

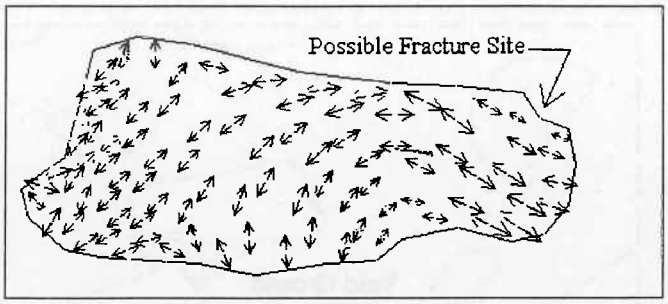

Figure 22. Principal Stress Vectors In Loaded Particle

3.2 initial Voids In FE Models With Perfect Particle / Matrix Bonding

As previously described in section 2.3, initial defects, such as flaws are an inevitable result of the processing route. To account for this effect FE models with initial damage were loaded similiar to the FE models discribed earlier. The main expected difference between these simulations and those of the previous sections is the fact that the void nucleation stage is now obselite and the failure mechanisim will be by void growth/coalesence. As before minimal damage occurred on the first load step but it was found that the maxiumum strain at the end of the first load step was alomst double that of the simulations without any initial defects. However, the strain at the end of the first load step did not exceed the 0.0014. Figure 23

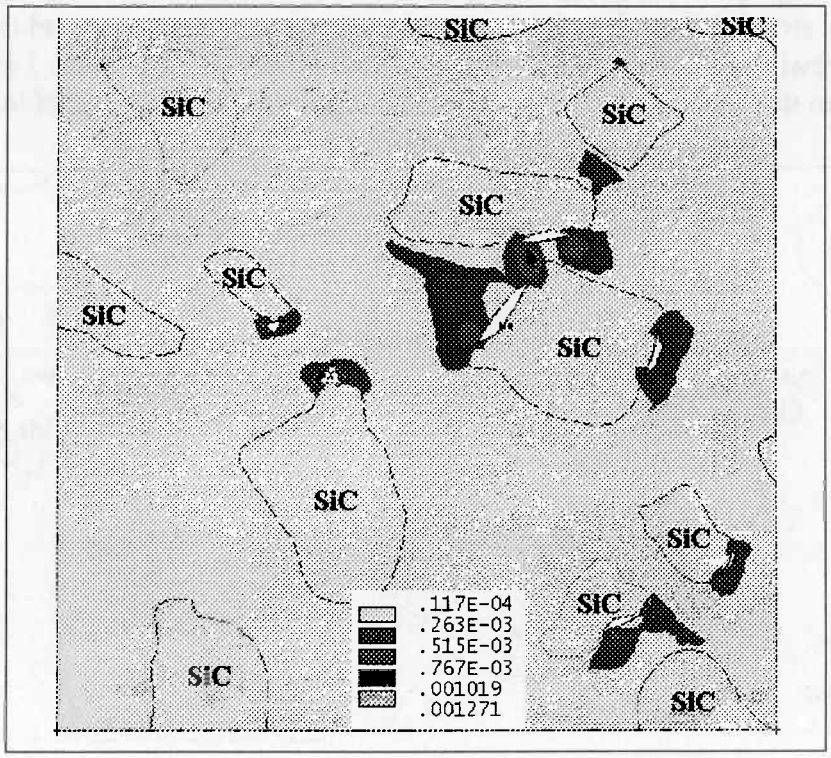

Figure 23. Strain Distribution For Load Step 1 Of MMC With Initial Voids

shows the strain distribution at the end of the first load step. It can be seen that the accumaltion of strain occurs around the initial voids and this increases rapidly with increasing load. At this load level of hydrostaic pressure a good indication can be gained into the prabole location and direction of void growth. After load step 2 the maximum strain increased by a factor of almost 4. Associated with this increase in load was over the straining of some

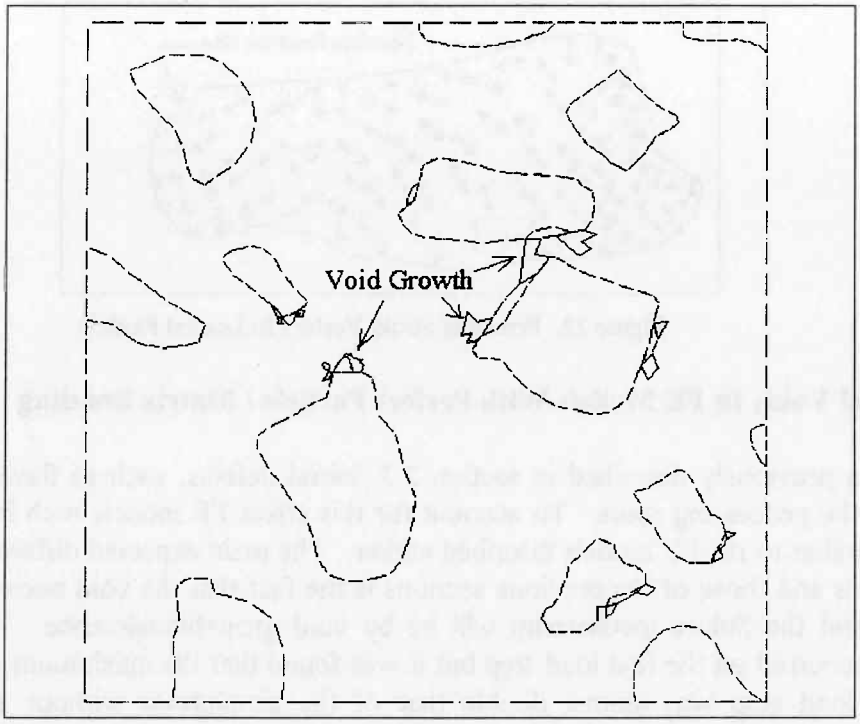

Figure 24. Void Growth At Load Step 2 For MMC With Initial Defects

elements. Figure 24 shows the void growth (elements killed) after load step 2. As can be seen the initally strained areas from load step 1 have become overstrained and this consequently lead to void growth. Figure 25 and 26 show the void growth for load steps 3 and 6 respectively. It can be seen that the sub surface damage is quite substantial at the end of load step 6. This

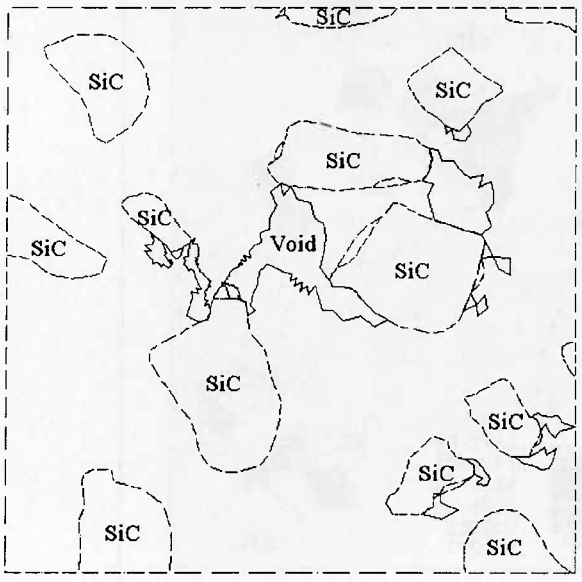

Figure 25. Void Growth For Load Step 3

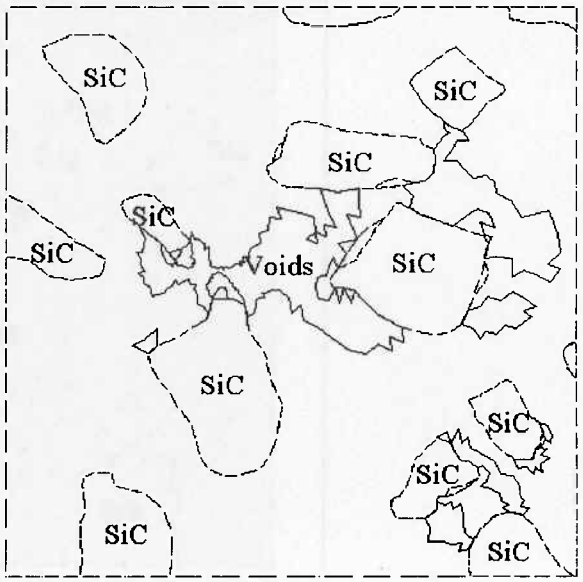

Figure 26. Void Growth For Load Step 6

damage is a direct result of the initial defects that existed at the particle/matrix interface prior to loading. Furthermore, the problem was aggrevated by the fact that the particles had clustered in a region thus causing an increase in the intensity tria-axial stress. It can also be seen that in regions without initial defects or particle clustering the particle remained bounded to the interface throughout the load steps. This may not have been the if account was taken

of the fact that the particle may slide within the matrix at high temperatures. Zahl and McMeeking [30] carried out FE simulations on PRMMC's with and without a sliding interface and concluded that for particles with aspect ratio's up to 2 the sliding interface had little effect on the composite strength. The sensitivity to interfacial sliding is more prounced for reinforcnments that corrospond to whisker or fibre reinforcement. Give that the maximum aspect ratio for the current simulationas was 3 it is felt that a sliding interface would have a negligable efect on the void growth rate provided that no initial voids existed. However, with initial defects at the interface particle sliding may adversely effect the strength of the composite. One model for estimating the void growth rate is that propsoed by Rice and Tracey [31]. The rate of volume growth for spherical diliation is given by

$$\frac{\dot{d}_O}{d_O} = 0.283\dot{\varepsilon}\exp\left(\frac{\sigma_1+\sigma_2+\sigma_3}{2\sigma_{YM}}\right) \tag{17}$$

where ε is the far field strain rate, σ_1, σ_2 and σ_3 describe the stress state at the void and σ_{YM} is the matrix yield stress. Generally it can be concluded that increasing the stress state at the particle/void will increase the rate of void growth. Therefore allowing the interface to slide will relax the stress state somewhat in the absence of initial defects. Figure 27 shows the equivalent stress distribution at sub model location 6 with initial defects. It can be seen that the maximum equivalent stress occurs in and around one of the particles in the cluster. Given that the matrix 0.1% yield strength is approximately 74 MPa a substantial amount of local yielding has occurred in the region of the clustered particle, while for the isolated particles little or no matrix yielding has occurred.

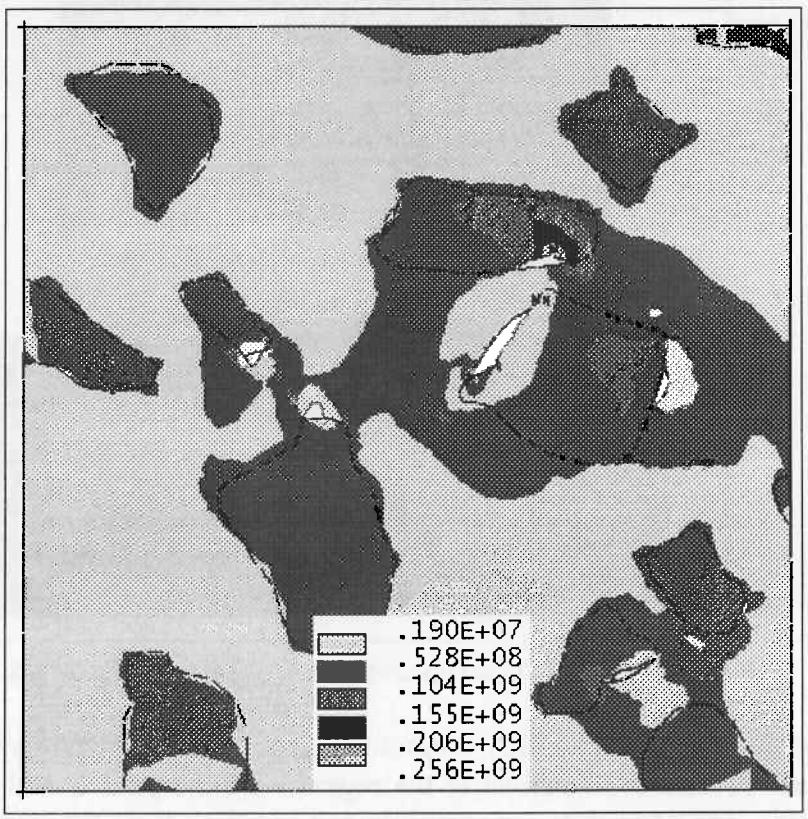

Figure 27. Von Mises Equivalent Stress Distribution At Sub Model Location 6

3.3 Wear Analysis

The wear simulation was a quantitative analysis performed in an effort to understand the wear mechanisms occurring during machining of PRMMC's. The FE model, figure 12, was used to describe the effect protruding SiC particles in the flowing chip would have on the tungsten carbide cutting tool. A normal displacement was applied to the MMC square while the tungsten carbide tool was held rigidly in place. Figure 28 depicts the predicted normal and shear stress distribution along the rake face of a cutting tool. At the nose radius the normal stresses are a maximum, it is in this region of very high normal stresses that sticking friction between the tool and the material occurs. Figure 29 shows the normal stress distribution in the MMC and the tungsten carbide in contact. Since the particle approximates to a circle in contact with a surface, it allows a comparisonto be made between thses and those

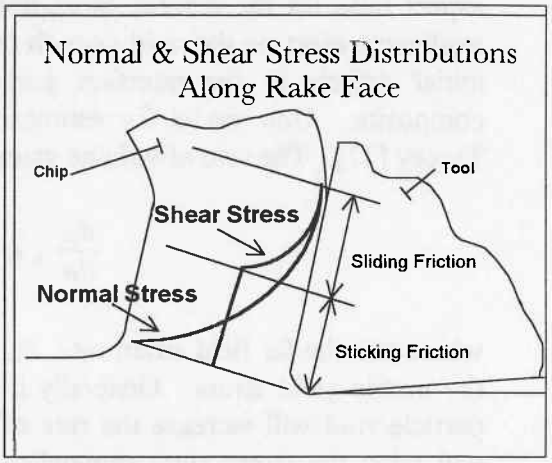

Figure 28. Stresses Along Rake Face

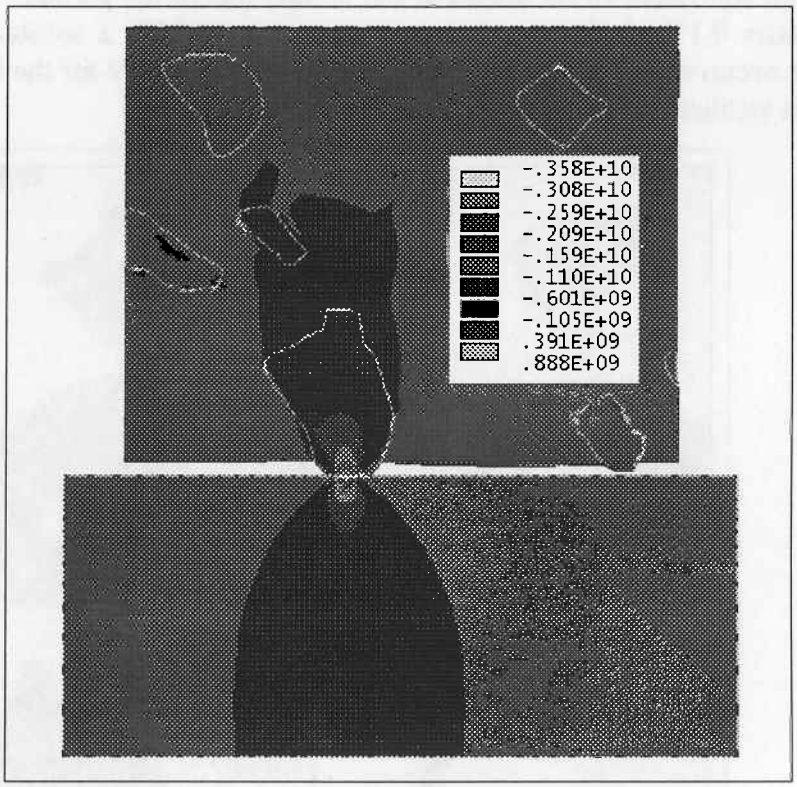

Figure 29. Normal Stress Distribution In MMC & Tungsten Carbide Model

predicted by Hertzian theory. This stress distribution is as predicted by Hertzian theory, that is, the normal stresses are localised at the region were the particle and the tungsten carbide make contact. The equivalent stress distribution resulting from the normal load is shown in Figure 30. It can be seen that the maximum equivalent stress occurs in the SiC particle in contact with the tungsten carbide. The magnitude of this maximum stress is approaching that

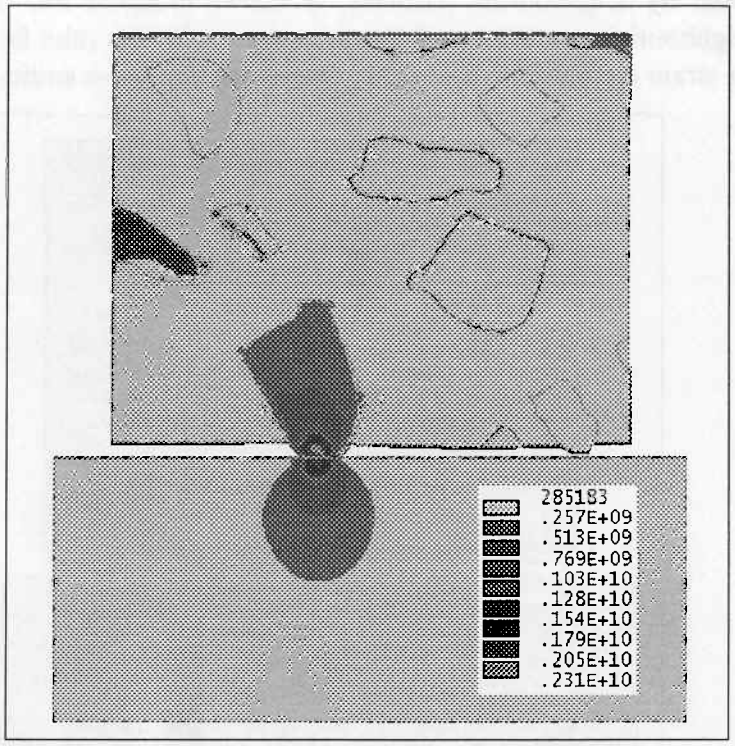

Figure 29. Equivalent Stress Distribution In MMC And Tungsten Carbide

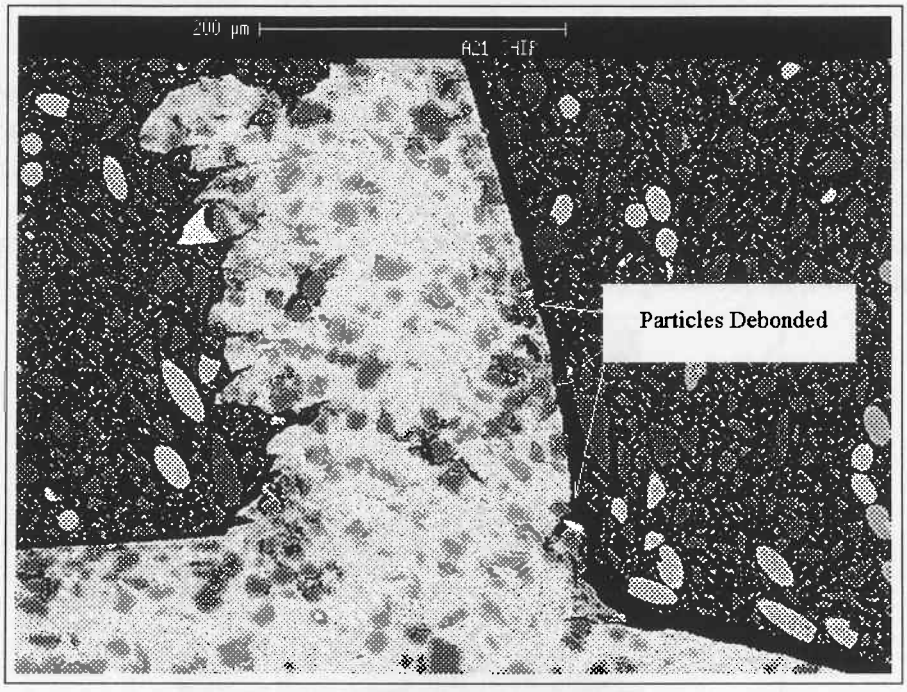

Figure 30. Chip Root Sample Obtained During Machining Of PRMMC With Tungsten Carbide Insert

of the strength of the SiC, hence under the action of the normal loading their is a tendency for the particle to fracture. However it is felt that particle rotation would occur given the viscosity of the matrix material in the region of the tool tip. This appears to be what occurs during actual machining, as shown in figure 30. The chip root shows extensive particles debonded from the particles that where in contact with, or sliding up, the rake face of the cutting tool. It can also be seen in figure 29, that the SiC particle in contact with the tungsten carbide carries the majority of the load. This excessive loading on the SiC particle due to contact can be

shared somewhat by neighbouring particles, as shown in figure 29. Furthermore, figure 30 shows that neighbouring particles to those in contact with the rake face have debonded also. The equivalent strain distribution, figure 31, shows that excessive strain occurs along the

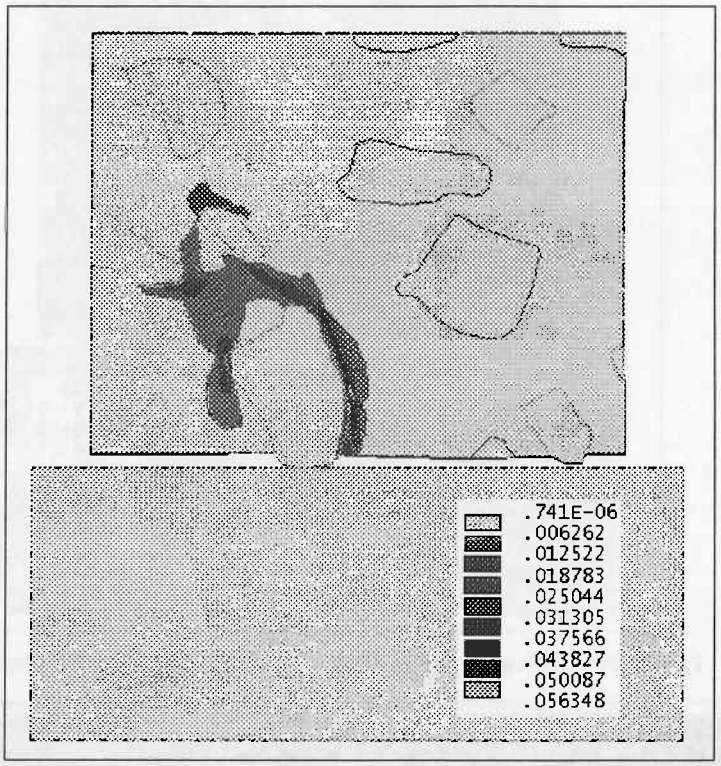

Figure 31. Strain Distribution Throughout The MMC and Tungsten Carbide

matrix/particle interface for up around the particle in contact. This strain is above the fracture strain of the matrix material (0.004) and therefore has failed and can no longer support any load. Considering the previous failure strain of the matrix material all the darker shaded regions shown in figure 31 would have failed and formed a void. This pattern of failure is again similar to that occurring during machining, figure 30.

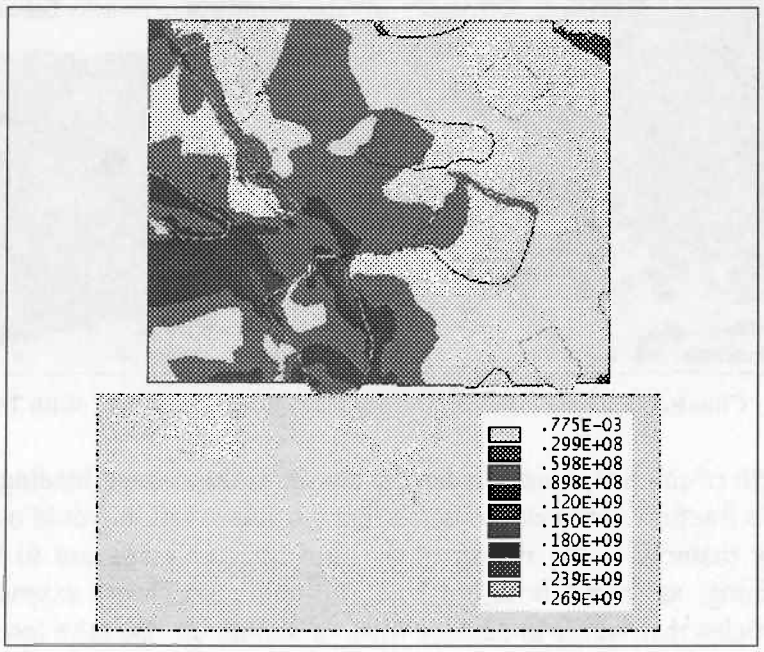

Figure 32. Equivalent Stress Distribution Throughout MMC And Tungsten Carbide

The second load step of the wear analysis was to fix the MMC square in the normal direction but to displace it tangentially relative to the tungsten carbide. This simulation was done in order to establish the effect tangential displacements would have on the stress within the composite. Figure 32 depicts the equivalent stress distribution for such a tangential displacement. It can be seen that the stresses have been redistributed within the matrix material around the particles in contrast to concentrating in the particles as with the normal

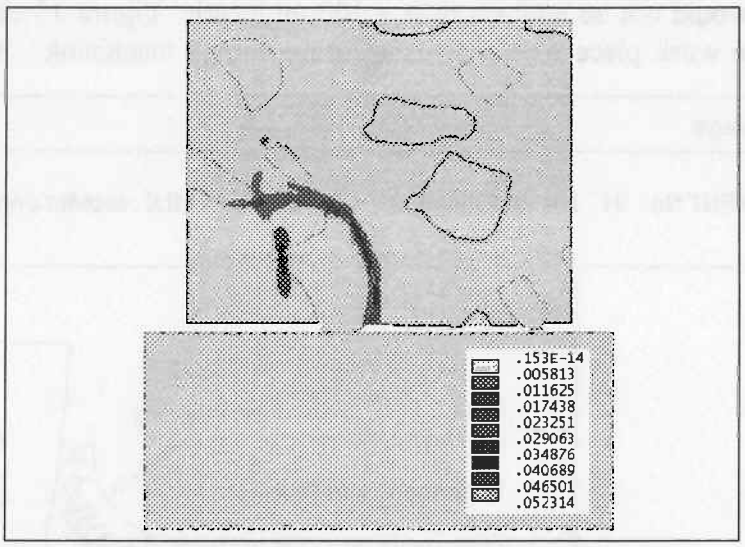

Figure 33. Strain Distribution Throughout The MMC and Tungsten Carbide

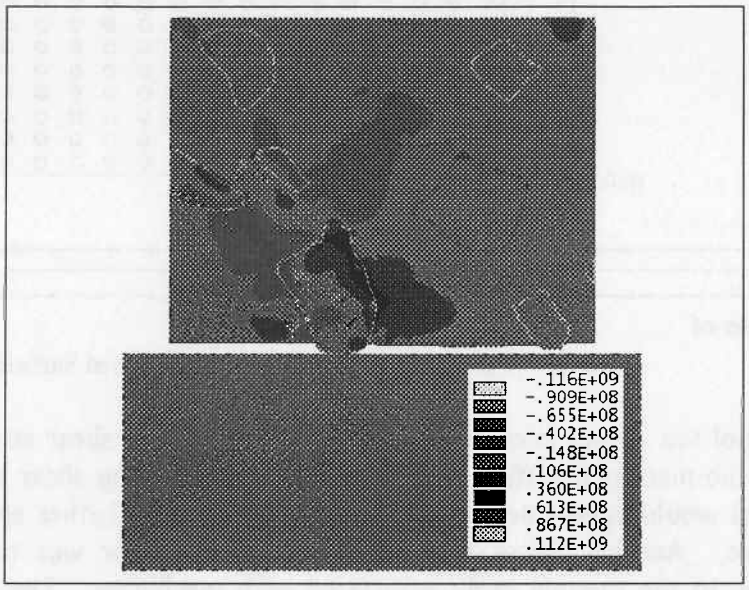

Figure 34. Shear Stress Distribution Throughout The MMC and Tungsten Carbide

loading, figure 29. The stress has now spread over a larger area of the MMC compared to that associated with the normal loading, and strain within the MMC as a result of the tangential displacement has only relaxed slightly. The location of the maximum strain is shown in figure 33 and is seen to be similar to that associated with the normal loading, figure 31. Figure 34 shows the shear stress distribution after the tangential loading was applied. Throughout the tungsten carbide tool the shear stresses are tensile and their magnitude is approximately 80-100 MPa. These tensile shear stresses within the tooling can cause mode II type crack propagation and are generally detrimental to the life of the tool.

4.0 COMMENTS & CONCLUSIONS

This paper has effectively shown how a complex micro mechanical process can be modelled by use of a sub modelling technique. One of the major assumptions made in the micro mechanical modelled approach was that the 100μm square was loaded by means of different values of hydrostatic pressure. During actual machining the stress / strain distributions would not be uniform over a 100μm length. Figure 35 shows how initial circles scribed on the work piece would deform during normal machining. It can be seen that just

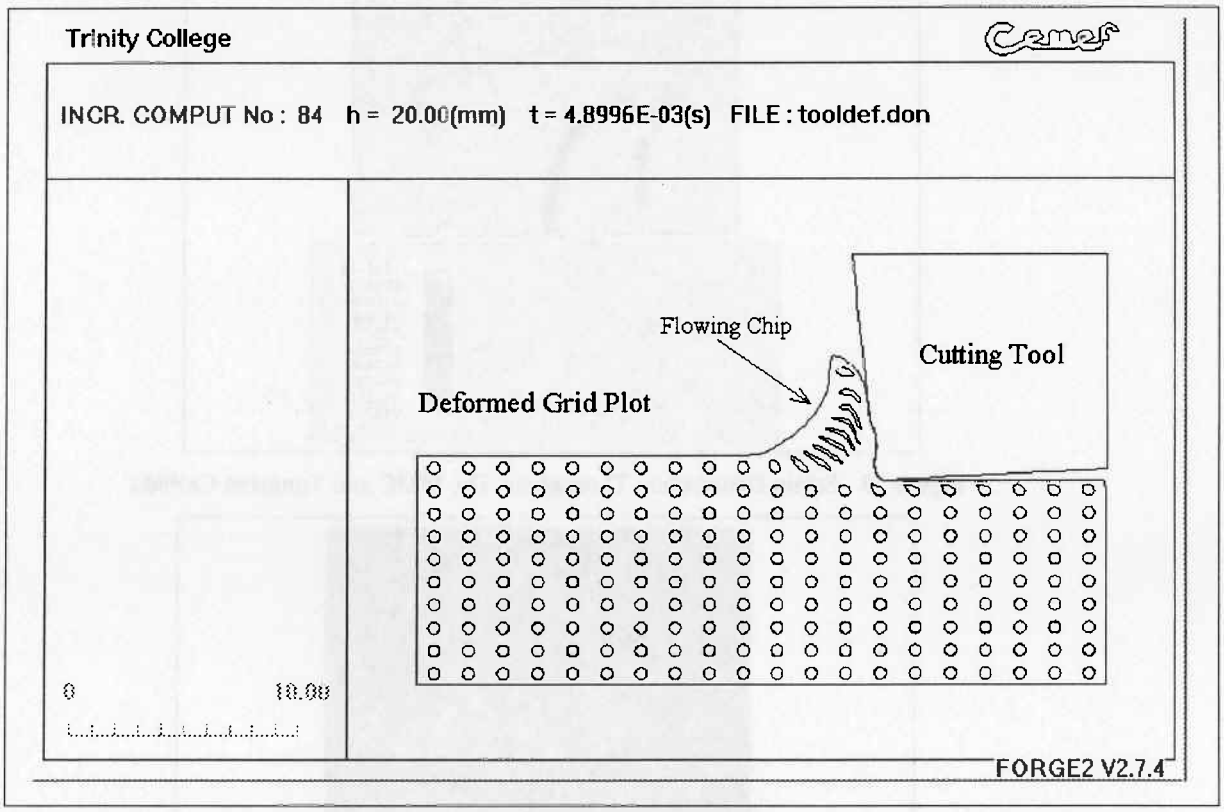

below the nose of

Figure 35. Deformed Circle Plot Over Machined Surface

the cutting tool the circles become distorted, indicating that shear stresses are acting to this depth below the machined surface. It is believed that applying shear loads along the sides of the sub-model would aggravate the void nucleation process further and would accelerate the rate of failure. Another factor that was not accounted for was that of residual stresses generated due to the thermal cycle associated with machining. The predicted temperatures associated with the machining of the A356 alloy are shown in figure 36. The maximum temperatures generated due to friction and visco plastic deformation were approximately 172°C. Assuming room temperature to be 20°C gives a temperature difference of 152°C. Takeo and Taya [31] applied the Eshelby equivalent strain model to obtain the residual stresses produced by thermal misfit in a particle reinforced composite, the particle is assumed to be spherical in shape and no plastic relaxation of stresses are accounted for. The residual stress in the particle, σ_p, is given by

$$\sigma_p = -\tfrac{2}{3}(1-f)\frac{E}{(1-\upsilon)\varepsilon^*} \qquad (18)$$

where f is the volume fraction, E and ν are the Young's modulus and Poission's ratio of the matrix respectively. ε^* is the eigen strain given by

$$\varepsilon^* = \frac{3m\Delta\alpha\Delta T}{\left[\frac{(1-f)(m+2)(1+\upsilon)}{(1+\upsilon)}\right]} + 3mf \tag{19}$$

and

$$m = \frac{(1+\nu)E_p}{(1-2\nu_p)E} \tag{20}$$

where the subscript p refers to the particulate, and $\Delta\alpha$ is the difference in coefficients of thermal expansion. The residual stress in the matrix, σ_m, is given by

$$\sigma_m = -\left[\frac{f}{1-f}\right]\sigma_p \tag{21}$$

Using the numerical values for the material constants was used in the FE simulations gives values for the residual stress of -371MPa and 200MPa in the particle and matrix respectively. It can be seen that the residual stresses in the particles are compressive and tensile in the matrix. The

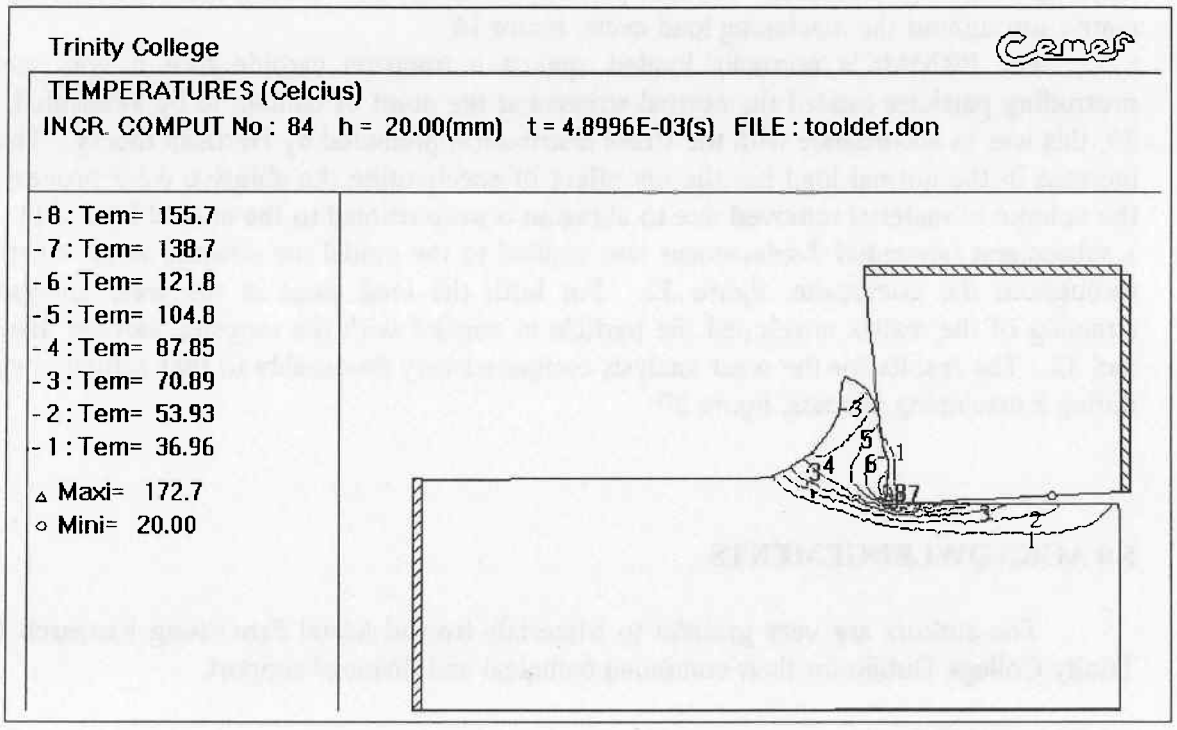

Figure 36. Temperature Distribution Obtained From FORGE2 Simulation

tensile stresses in the matrix would again have aggravated the damage accumulation rate. It should be noted that the predicted value of tensile stress does not account of plastic relaxation processes which would reduce the stress. The compressive stress in the particle would act to close and initial cracks or flaws in the particles and reduce further the likelyhood of particle fracture during machining.

It can be concluded from the current simulations that the presence of initial defects in the microstructure have a very detrimental effect on the damage accumulation rate of the

It can be concluded from the current simulations that the presence of initial defects in the microstructure have a very detrimental effect on the damage accumulation rate of the composite during machining, figure 26. The primary reason for this is that the normal failure mechanism associated with PRMMC's is through void nucleation, propagation and coalesence. With initial defects in the microstructure the first of these stages, nucleation, is absent so the rate of damage accumulation is accelerated. A similar analogy can be drawn from the fatigue of steel. The crack initiation period is normally the longest and in its absence the time or number of cycles to failure is greatly reduced. The region just at the cutting tool nose radius is the region where the majority of damage occurs during the machining of PRMMC's, figure 15 shows how the void propagation process is accelerated in this region. The main reason for this is that approaching this region the material is in a state of compression but on passing the tool nose radius the material stress state is reversed and becomes tensile, figure 6. This tensile stress field had the greatest detrimental effect on the PRMMC with initial voids, the equivalent stress was shown to almost doubled, figure 27 and the amount of damage is considerably greater, figures 16 and 26.

Particle/matrix debonding was favoured at flat planes on particles where their was an intensification of hydrostatic stresses, figure 17. However debonding also occurred at particle corners with no initial defects because the stress was concentrated there, thereby causing premature debonding. Particle clustering caused a further increase in the state of stress due to applied loading, this was reinforced by the fact that it was at the particle clusters that the majority of damage occurred. Remote particles without initial defects remained bonded to the matrix throughout the machining load cycle, figure 16.

For PRMMC's normally loaded against a tungsten carbide face it was seen that protruding particles caused the normal stresses at the point of contact to be intensified, figure 29, this was in accordance with the stress distribution predicted by Hertzian theory. This local increase in the normal load has the net effect of accelerating the abrasive wear process, since the volume of material removed due to abrasion is proportional to the normal load [31]. When a subsequent tangential displacement was applied to the model the stresses were redistributed throughout the composite, figure 32. For both the load steps in the wear analysis over straining of the matrix enveloped the particle in contact with the tungsten carbide, figures 31 and 33. The results for the wear analysis compared very favourably to that actually occurring during a machining process, figure 30.

5.0 ACKNOWLEDGEMENTS

The authors are very grateful to Materials Ireland Metal Processing Research Unit at Trinity College Dublin for their continued technical and financial support.

6.0 REFERENCES

1. J. Charbonnier, S. Dermarker, M. Santarini, J. Fages and M. Sabatie, High Performance Metal Matrix Composites Manufactured by Squeeze Casting, ibid., pp. 127-132 1988.
2. S. P. Waldrop Metal Matrix Composites: Manufacturing Challenges. SME Technical Paper EM85-106, Composites In Manufacturing 4 Conference, Jan, 1985, California.
3. G.L. Povirk, A. Needleman and S.R. Nutt, An Analysis of the effect of residual stresses on deformation and damage mechanisms in Al-SiC composites, Materials Science and Engineering, A132, 1991, pp. 31-38.

4. A.P. Divecha, S.G. Fishman, and S.D. Karmarker, Silicon Carbide Reinforced Aluminium-A Formable Composite, Journal Of Metals, Sept. 1981, pp.12-17.
5. O. Quigley, J. Monaghan, P.O'Reilly, Factors affecting the machinibility of an Al/SiC metal-matrix composite, Journal of Material Processing Technology, 43 (1994), pp.21-36.
6. D. Brazil, J. Monaghan, An Investigation of the cutting mechanism associated with the machining of an Al/SiC Metal Matrix Composite, IMC12, Competitive Manufacturing, Sept.1995.
7. Hashemi, J., Tseng, A. A., and Chou, P. C., Finite Element Modelling of Segmented Chip Formation in High Speed Orthogonal Cutting, J. of Mat. Eng. and Performance, Vol 3 (5) Dec., 1994, pp 712-721.
8. Marusich, T.D., and Ortiz, M., Simulation of Chip Formation in High Speed Machining, AMD Vol 208/MD Vol.59, Machining Of Advanced Materials, ASME 1995.
9. Strnkowski, J. S., and Carrol, J. T., A finite Element Simulation Of Orthogonal Metal Cutting, J. Of Eng. for Ind., Vol.117, 1985, pp 346-354.
10. Shih, A. J., Finite Element Simulation of Orthogonal Metal Cutting, Trans. of ASME, Vol.117, Feb., 1995, pp84-93.
11. Sekhon, G. S., and Chenot, J. L., Numerical Methods In Industrial Forming Processes, Chenot, Wood and Zienkiewicz (eds.), 1992, Balkema, Rotterdam, ISBN 9054100877.
12. Bellet, M et al (eds.), Plasticity and Metal Forming, Sophia Antipolis, 1990.
13. FORGE2 Reference Manual, Transvalour, Sophia Antipolis.
14. C.K.H. Dharan and S. Kobayashi, Forming of Metal Matrix Composites, Numerical Modelling of Material Deformation processes, P. Hartley, I. Pillinger and C. Sturgess (Eds.) pp.358.
15. V. Tvergaard, Effect of Fibre Debonding in a Whisker Reinforced Metal, Material Science and Engineering, A125, 1990, pp.203-213.
16. G.L. Roy, J. Embury, G. Edwards and M.F. Ashby, A Model of Ductile Fracture Based on Nucleation and Growth of Voids, Acta Metall., 29, 1981, pp.1509-22.
17. L. M. Brown and W. M. Stobbs, The Work Hardening of Cu-SiO_2 V. Equilibrium Plastic Relaxation by Secondary Dislocations, Phil. Mag., 34, 1976, pp.351-72.
18. S. H. Goods and L. M. Brown, The Nucleation of Cavities by Plastic Deformation, Acta Metall., 27, 1979, pp.1-15.
19. J.C. Lee, K.N. Subramanian, Failure Behaviour of particulate-reinforced aluminium alloy composites under uniaxial tension, J. Of Materials Science, 27, 1992, pp.5453-5462.
20. Y. Flom and R.J. Arsenault, Mater. Sci. Engng. 77, 1986, pp.191.
21. J.J Lewandowski, C. Liu, W.H. Hunt, Effects of Matrix Microstructure and Particle Distribution on Fracture of an Aluminium Metal Matrix Composite, Materials Science and Engineering, A107, 1989, pp.241-255.
22. A.F. Whitehouse, R.A. Shahani and T.W. Clyne, Cavitation during tensile deformation of powder route particle reinforced MMC's, in Metal Matrix Composites: Processing, Microstructure and Properties, 12th Riso Nat. Lab., Denmark, 1991, pp.741-8.
23. I.M Hutchings, Tribology-Friction and Wear of Engineering Materials, Edward Arnold (Eds.) 1992, pp143.
24. J.C. Lee, K.N. Subramanian, Failure Behaviour of particulate-reinforced aluminium alloy composites under uniaxial tension, J. Of Materials Science, 27, 1992, pp.5453-5462.
25. A.K. Vasudevan, O. Richmond, F. Zok and J.D. Embury, The influence of Hydrostatic Pressure on the Ductility of Al-SiC Composites, Materials Science and Engineering, A107, 1989, pp.63-69.
26. W.F Hosford and R.M. Caddell, Metal forming-Mechanics and Metallurgy, pp.123, Prentice-Hall, Englewood Cliffs, N.J. 1983.

27. R. Hill, The Mathematical Theory of Plasticity, pp.330, Science Series Clarendon Press, Oxford, 1986.
28. D. Lloyd, Aspects of particle fracture in particulate reinforced MMC's, Acta Met et. Mat., 39, 1991, pp.59-72.
29. H.L. Cox The elasticity and strength of paper and other fibrous materials, Brit. j. Appl. Physics, 3, 1952, pp.73-79.
30. D.B. Zahl, R.M. Mcmeeking, The effect of interfacial properties on the flow strength of discontinuous reinforced metal matrix composites, Mechanics of Composite Materials and Structures, Vol. 1, 1994, pp.31-52.
31. J. Rice, D.M. Tracey, On the ductile enlargement of voids in triaxial stress fields, J.Mech. Phys. Solids, 17, 1969, pp201-217.